iScience

CellPress
OPEN ACCESS

Article

A long intergenic non-coding RNA regulates nuclear localization of DNA methyl transferase-1

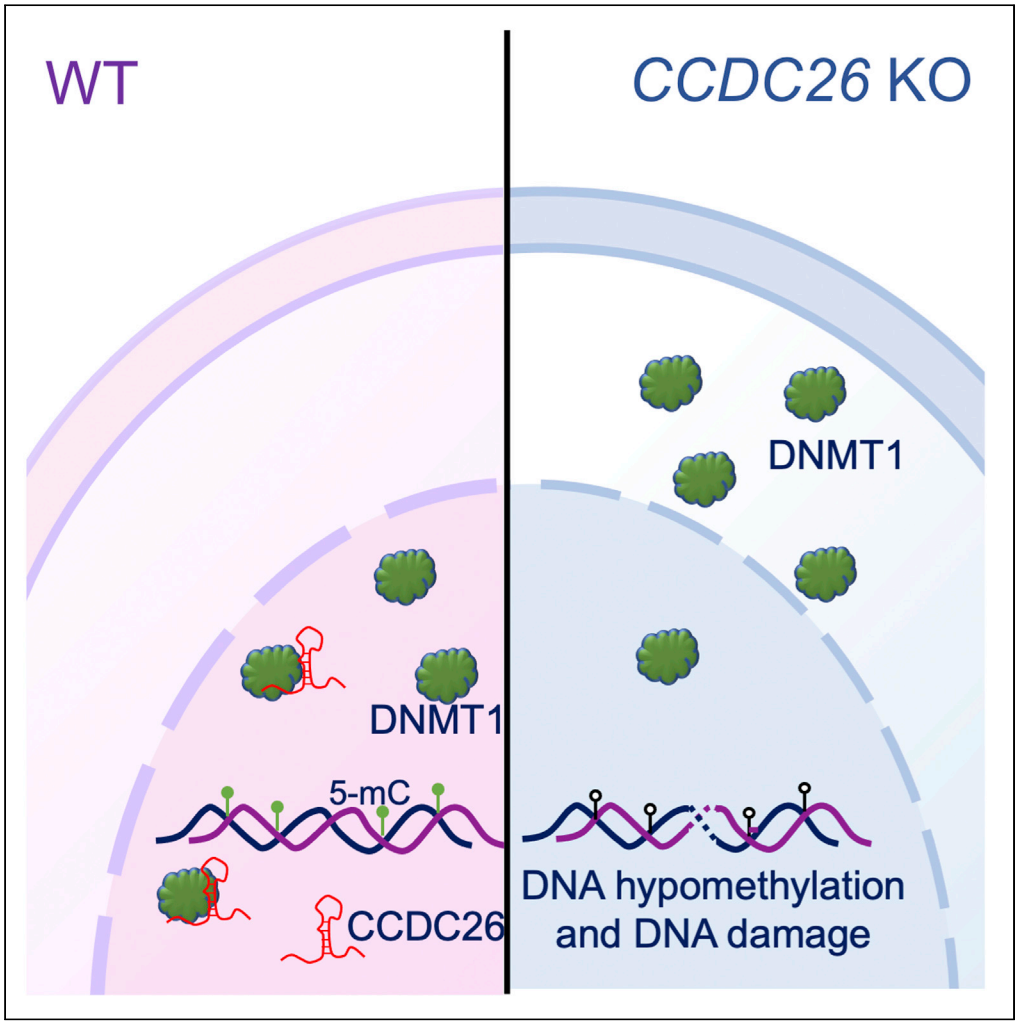

Rhian Jones, Susanne Wijesinghe, Claire Wilson, John Halsall, Triantafillos Liloglou, Aditi Kanhere

a.kanhere@liverpool.ac.uk

Highlights

LincRNA CCDC26 influences cellular localization of the enzyme DNMT1

In the absence of CCDC26, the genomic DNA is significantly hypomethylated

Removal of CCDC26 leads to double-stranded DNA breaks and increased cell death

Jones et al., iScience 24, 102273
April 23, 2021
https://doi.org/10.1016/j.isci.2021.102273

iScience

CellPress
OPEN ACCESS

Article

A long intergenic non-coding RNA regulates nuclear localization of DNA methyl transferase-1

Rhian Jones,[1] Susanne Wijesinghe,[2] Claire Wilson,[3] John Halsall,[4] Triantafillos Liloglou,[3] and Aditi Kanhere[1,3,5,6,*]

SUMMARY

DNA methyl transferase-1 or DNMT1 maintains DNA methylation in the genome and is important for regulating gene expression in cells. Aberrant changes in DNMT1 activity and DNA methylation are commonly observed in cancers and many other diseases. Recently, a number of long intergenic non-protein-coding RNAs or lincRNAs have been shown to play a role in regulating DNMT1 activity. *CCDC26* is a nuclear lincRNA that is frequently mutated in cancers and is a hotbed for disease-associated single nucleotide changes. However, the functional mechanism of *CCDC26* is not understood. Here, we show that this lincRNA is concentrated on the nuclear periphery. Strikingly, in the absence of *CCDC26* lincRNA, DNMT1 is mis-located in the cytoplasm, and the genomic DNA is significantly hypomethylated. This is accompanied by double-stranded DNA breaks and increased cell death. These results point to a previously unrecognized mechanism of lincRNA-mediated subcellular localization of DNMT1 and regulation of DNA methylation.

INTRODUCTION

In the mammalian genome, DNA is often methylated at cytosines in CpG dinucleotides. DNA methylation is one of the important epigenetic modifications needed for transcriptional regulation of genes (Jaenisch and Bird, 2003). This modification plays a crucial role in many vital cellular processes such as heterochromatin formation, X-chromosomal inactivation, and genomic stability (Csankovszki et al., 2001; Nan et al., 1998; Watt and Molloy, 1988). Unsurprisingly, aberrant DNA methylation is implicated in many diseases and developmental defects (Baets et al., 2015; Daskalos et al., 2009; Eden et al., 2003; Gaudet et al., 2003; Heller et al., 2016; Klein et al., 2013; Morgan et al., 2018; Pakneshan et al., 2004; Schmelz et al., 2005; Stirzaker et al., 1997; Wen et al., 2018; Yu et al., 2013). Regulation of DNA methylation is therefore crucial throughout mammalian existence.

In mammals, DNMT3a, DNMT3b, and DNMT1 are DNA methyltransferases that are responsible for establishing and maintaining genomic methylation in cells (Lyko, 2018). DNMT3a and DNMT3b are primarily involved in establishing *de novo* DNA methylation patterns in the genome. In the very early stages of development, DNA methylation is completely eradicated in primordial germ cells, resulting in an epigenetically "blank canvas." The DNMT3s then restore DNA methylation in a non-CpG-specific and ubiquitous manner (Doherty et al., 2002; Otani et al., 2009; Rasmussen and Helin, 2016). In contrast, DNMT1 plays a more predominant role in maintaining post-replicative methylation patterns, by preferentially binding hemi-methylated DNA, and methylating the newly synthesized daughter strand (Lyko, 2018). At late S-phase of the cell cycle, DNMT1 is targeted to replication foci, a process dependent on an additional ubiquitin-like protein, with PHD and RING finger domains 1 (UHRF1) (Berkyurek et al., 2014; Bostick et al., 2007; Bronner et al., 2019). Evidence suggests that during the replication process, DNMT1 also interacts with histone-modifying enzymes such as histone deacetylase HDAC2 as well as histone methyltransferases, EZH2 and G9a (Esteve et al., 2006; Rountree et al., 2000; Wang et al., 2017).

Aberrant DNA methylation is suspected to play a role in many cancers, e.g., hepatocellular carcinoma, glioblastoma, breast cancer, squamous cell lung cancer, thyroid cancer, and leukemia, (Daskalos et al., 2009; Eden et al., 2003; Gaudet et al., 2003; Heller et al., 2016; Morgan et al., 2018; Pakneshan et al., 2004;

[1]School of Biosciences, University of Birmingham, Edgbaston, Birmingham, UK

[2]Institute of Inflammation and Ageing, University of Birmingham, Edgbaston, Birmingham, UK

[3]Institute of Systems, Molecular and Integrative Biology, University of Liverpool, Liverpool, UK

[4]Institute of Genomic Sciences, University of Birmingham, Edgbaston, Birmingham, UK

[5]Present address: Department of Molecular Physiology and Cell Signaling, Institute of Systems, Molecular and Integrative Biology, University of Liverpool, Crown Street, Liverpool, L69 3BX, UK

[6]Lead contact

*Correspondence: a.kanhere@liverpool.ac.uk

https://doi.org/10.1016/j.isci.2021.102273

Schmelz et al., 2005; Stirzaker et al., 1997; Wen et al., 2018; Yu et al., 2013), and DNMT mutations are also the cause of developmental diseases such as hereditary sensory and autonomic neuropathy type 1E (HSAN1E) (Baets et al., 2015; Klein et al., 2013).

In somatic cells, DNMT1 is the most abundant and most active methyl transferase. It is a predominantly nuclear protein with an N-terminal nuclear localization signal (NLS) stretching between 177 and 205 amino acid residues (Alvarez-Ponce et al., 2018). The N-terminus of DNMT1 also contains domains required for its interaction with partner proteins, including DMAP1, HP1, G9a, and PCNA (Esteve et al., 2006; Fuks et al., 2003; Iida et al., 2002; Rountree et al., 2000). The central region of DNMT1 is needed for its targeting to replication foci (Leonhardt et al., 1992), whereas the C-terminus comprises the catalytic domain required for methyl-transferase activity (Song et al., 2012).

A number of studies have shown that DNA methylation is regulated by non-protein-coding RNAs or ncRNAs (Berghoff et al., 2013; Imamura et al., 2004; Jeffery and Nakielny, 2004; Yu et al., 2008). Also, DNMT1 function is often influenced by its interactions with ncRNAs. Long ncRNAs or lncRNAs such as *KCNQ1OT1* (Mohammad et al., 2010), *Dali* (Chalei et al., 2014), *lincRNA-p21* (Bao et al., 2015), *PARTICLE* (O'Leary et al., 2017), *ecCEBP* (Di Ruscio et al., 2013), *DACOR1* (Somasundaram et al., 2018), and *HOXA11-AS1* (Guo et al., 2019) are shown to interact with DNMT1 and modulate its activity. Here we report an interaction between DNMT1 and a long intergenic non-coding RNA (lincRNA), *CCDC26*. LincRNA *CCDC26* is transcribed from a 328-kilobase gene on chromosome 8, from 8q24.21 locus neighboring the proto-oncogene c-MYC. The 8q24 locus is a hotbed for disease-associated mutations including cancer-associated SNPs and copy-number alterations (Wilson and Kanhere, 2021). It is of specific interest in acute myeloid leukemia (AML) because of the high-frequency occurrence of AML-associated mutations and variants in *CCDC26* gene (Duployez et al., 2018; Izadifard et al., 2018; Kuhn et al., 2012; Radtke et al., 2009). These observations suggest that *CCDC26* might play an important role in driving cancer progression. Previous studies show that *CCDC26* might be involved in regulating apoptosis and differentiation in myeloid cells (Yin et al., 2006; Hirano et al., 2015). However, the functional mechanism of *CCDC26* remains elusive.

In this study, we aimed to understand the function of *CCDC26* and its role in cancer. Here, we show that *CCDC26* interacts with DNMT1 and is predominantly localized on the nuclear periphery. In the absence of *CCDC26*, DNMT1 is mis-localized in the cytoplasm, leading to DNA hypomethylation and apoptosis similar to that observed on inhibition of DNMT1 in myeloid leukemia cells. As a result, we observe genome-wide changes in gene expression. LincRNA-mediated DNMT1 mis-localization has not been previously reported and has significant implications to DNA methylation regulation, as well as cancer and RNA biology.

RESULTS

LincRNA *CCDC26* is a myeloid-specific RNA expressed from second TSS

We first sought to understand the gene structure and expression pattern of *CCDC26*. Previous investigations (Hirano et al., 2015; Yin et al., 2006) on various cell types showed that *CCDC26* is highly expressed in myeloid leukemias. We further examined this by measuring *CCDC26* levels in a number of additional leukemia and non-leukemia lines (Figure S1A). In agreement with previous results, we observed that *CCDC26* is highly expressed in myeloid cells and is present at much lower levels in other cell types. We also observed that among myeloid cells the highest level of expression is in chronic myeloid cells, K562 (Figure S1A).

According to current gene annotations, altogether there are four isoforms of *CCDC26* that are transcribed from human chromosome 8 from two distinct transcription start sites, TSS1 and TSS2 (Figure 1A). These isoforms show alternative splicing patterns and contain combinations of six exons. Isoforms-1 (1666bp) and -2 (1649bp) are transcribed from an independent transcription start site (TSS2) and differ only by an additional 17 nucleotide sequence at the 3′ end of exon 4 in Isoform-1. Isoform-3 (1495bp), which is also transcribed from TSS2, lacks exon 4 completely. Isoform 4 (1718bp) is transcribed from TSS1, a start site that lies upstream of TSS2.

To understand which *CCDC26* isoforms are expressed in K562 cells, we carried out qRT-PCR measurements using isoform-specific primers (Figure 1B and Table S1). In these cells, the four isoforms of *CCDC26* are not

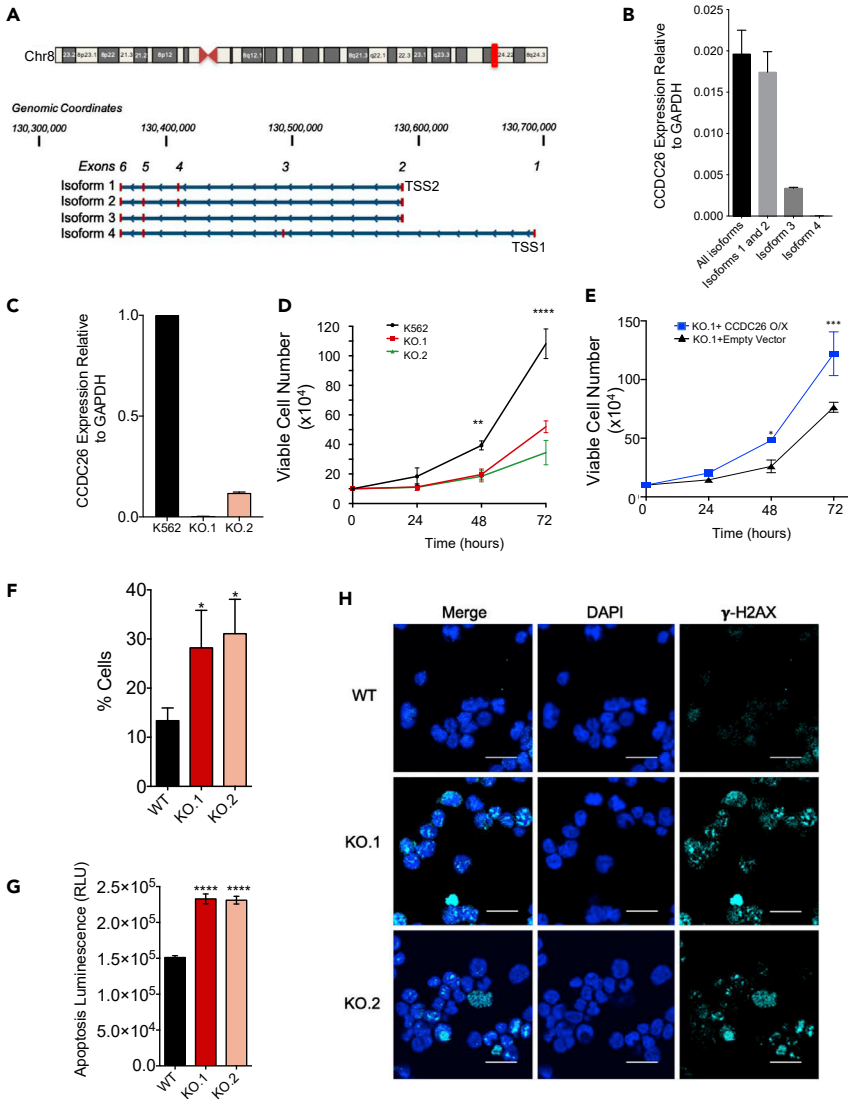

Figure 1. LincRNA *CCDC26* knockout results in slower growth and increased apoptosis and DNA damage in K562 cells

(A) A schematic diagram illustrating the four currently known isoforms of *CCDC26*, adapted from the UCSC Genome Browser view of the *CCDC26* locus (NCBI RefSeq tracks, GRCh37/hg19 assembly. Ideogram for chromosome 8 is shown at the top. The red baron ideogram indicates *CCDC26* position. *CCDC26* isoforms are transcribed from one of two transcription start sites (TSS-1 and TSS-2) located on Chr8q24 locus.

(B) A plot showing the RNA levels of different *CCDC26* isoforms, relative to GAPDH, in K562 cells, measured using qRT-PCR. Error bars represent the mean ± standard deviation.

(C) A plot showing *expression* level of *CCDC26* RNA relative to GAPDH in WT K562, KO.1, and KO.2 cells measured using qRT-PCR. *CCDC26* levels were significantly reduced in both knockouts. Error bars represent the mean ± standard deviation.

(D) Growth curve for WT K562, KO.1, and KO.2 cells showing slower growth in the latter cell lines. Values represent the mean ± standard deviation. *$p < 0.05$; **$p < 0.005$; ***$p < 0.001$; ****$p < 0.0001$ (unpaired, two-tailed t test, n = 3).

(E) Growth curve for KO.1 expressing *CCDC26* from exogeneous plasmid vector and KO.1 expressing empty vector. Values represent the mean ± standard deviation. *$p < 0.05$; **$p < 0.005$; ***$p < 0.001$; ****$p < 0.0001$ (unpaired, two-tailed t test, n = 3).

(F) A plot showing the percentage of apoptotic WT, KO.1, and KO.2 cells in the sub-G1 phase of the cell cycle according to propidium iodide FACS analysis. Values represent the mean ± standard deviation. *$p < 0.05$, **$p < 0.005$; ***$p < 0.001$; ****$p < 0.0001$ (unpaired, two-tailed t test, n = 3).

Figure 1. *Continued*

(G) The ApoTox-Glo assay allows for detection of apoptosis in cells. The Caspase-Glo 3/7 reagent results in cell lysis, leading to caspase cleavage and the release of the luciferase substrate amino-luciferin, causing the luciferase reaction to emit light, indicating apoptosis. Luminescence was detected and measured for WT and *CCDC26* KO cells to determine the level of apoptosis in cells. Values represent the mean ± standard deviation. *p < 0.05; **p < 0.005; ***p < 0.001; ****p < 0.0001 (unpaired, two-tailed t test, n = 5).

(H) Confocal images demonstrating the results of anti-γ-H2AX immunofluorescence. WT, KO.1, and KO.2 cells were stained with DAPI nuclear stain (blue) and anti-γ-H2AX antibody (cyan). Increased numbers of γ-H2AX foci are present in the KO cells. Scale bar, 25 um.

uniformly expressed. Isoforms starting from TSS2 i.e. isoforms-1, -2, and -3 account for more than 95% of the total *CCDC26* transcripts in the cell. Among the three isoforms starting at TSS2, Isoform-1 and Isoform-2 alone make 80% of *CCDC26*, whereas Isoform-3 is detected at considerably lower levels, accounting for only ∼15% of *CCDC26* expression. On the other hand, Isoform-4, which is expressed from another transcription start site, TSS1, is barely detectable (Figure 1B).

LincRNA *CCDC26* depletion leads to DNA damage and apoptosis

To further understand the role of *CCDC26* in myeloid cells, we carried out CRISPR-Cas9-mediated knockout (KO) of this lincRNA in K562 cells. Given that more than 99% of *CCDC26* is transcribed from TSS2, we simultaneously used two small guide RNAs to mutate TSS2 (Figure S1B). Following single-cell clonal expansion, we established two cell lines, KO.1 and KO.2, which exhibit ∼99% and ∼88% reduction in *CCDC26* levels, respectively (Figure 1C).

We first analyzed the effect of *CCDC26* knockout on cell growth. Interestingly, *CCDC26* depletion resulted in a significantly reduced rate of growth in both KO cell lines (Figure 1D). Cells were counted every 24 h across a 72 h period, and growth curves were subsequently plotted. Although wild-type (WT) cells double in number approximately every 24 h as previously reported (Murray et al., 1993), the number of KO cells only increase 2-fold approximately every 48 h (Figure 1D). A previous study (Hirano et al., 2015) also observed slower growth rate upon shRNA mediated knockdown of *CCDC26*. However, this effect was only observed under high serum conditions. The effect of *CCDC26* removal under normal growth conditions has not been reported before. Our results confirm that, even under normal conditions, *CCDC26* removal leads to reduced cell growth (Figure 1D). To further confirm this phenotype and to rule out the possibility that the slow growth in KO cells is a result of clonal selection after CRISPR knockouts, we compared the growth rates of KOs with clonal population transfected with CRISPR/Cas9 plasmid on its own without sgRNAs. However, this CRISPR control displayed similar growth rate as K562 cells (Figure S1C), supporting our observation that the slower growth rate observed in KOs is a likely consequence of *CCDC26* knockout and not a result of clonal isolation. We also reintroduced *CCDC26* in the knockouts using an exogenous plasmid vector. Overexpression of *CCDC26* in the knockouts increased cell growth rate as compared with knockouts that expressed an empty vector (Figures 1E and S1D), further supporting our observation that the cell growth changes are due to removal of *CCDC26*.

The slow growth observed in KO cells could be either because of changes in cell cycle or because of an increased rate of cell death. Previously, *CCDC26* has been implicated in apoptosis (Hirano et al., 2015; Yin et al., 2006); however, its effect on cell cycle has not been investigated. To understand the reason behind slow growth rate in KO cells, we subsequently analyzed cell-cycle progression in WT and KOs by incorporation of propidium iodide and subsequent FACS analysis. This method measures the number of DNA strands to determine cell cycle progression. We did not observe any significant changes in any of the key cell-cycle stages (Figures S1E–S1G). However, cell cycle analysis showed an increased population of *CCDC26* KO cells in the sub-G1 state, which is indicative of apoptosis (Figure 1F). Cell cytotoxicity and apoptosis assays that measure caspase levels also confirmed that in comparison to WT, *CCDC26* KO cells were less viable and more apoptotic (Figure 1G). The process of apoptosis is often linked to DNA damage. Hence, we explored the possibility of increased DNA damage in *CCDC26* KO cells. We tested for increased presence of histone variant γ-H2AX (Figure 1H). Histone variant H2AX is key in the cellular response to DNA damage, as its C-terminal tail is rapidly phosphorylated at a Serine residue following the occurrence of a DNA double-strand break (DSB). Phosphorylated H2AX or γ-H2AX is used as a DSB marker and can be readily detected by anti- γ-H2AX antibody (Rogakou et al., 1998). A visible increase in γ-H2AX foci was observed in both *CCDC26* KO lines as compared with WT cells (Figure 1H and Tables S2 and S3). Together, these results indicated that removal of *CCDC26* results in DNA damage, apoptosis, and slow growth.

Absence of *CCDC26* leads to DNMT1 mis-localization and DNA hypomethylation

We further sought to understand the mechanism behind *CCDC26*-mediated DNA damage. We first enquired if this RNA influences genomic DNA and chromatin in any other way. Many lncRNAs are involved in regulation of chromatin modifications (Di Ruscio et al., 2013; Mohammad et al., 2010; Pandey et al., 2008; Rinn et al., 2007). We speculated that *CCDC26* might also function by regulating changes in epigenetic modifications. In order to verify this, we tested global genomic levels of multiple common histone modifications such as H3K27me3, H3K27ac, H3K9me3, H3K9ac, and H4K16ac using immunoblotting (Figure S2). However, we did not see any significant changes in genomic levels of tested histone modifications in *CCDC26* KO cells. Using immunoblotting, we also tested levels of histone-modifying enzymes such as EZH2, G9a, and HDAC2 (Figure S2) that are involved in catalyzing these modifications. However, similar to histone modifications, levels of these catalytic proteins did not show any changes. Although this observation does not rule out possibility of site-specific variations in histone modifications, these results indicate that absence of *CCDC26* did not lead to any significant changes in overall levels of histone modifications or the enzymes that catalyze these histone modifications.

In addition to histone modifications, DNA methylation is an important epigenetic modification. Importantly, DNA methylation is also shown to be regulated by various lncRNAs (Bao et al., 2015; Chalei et al., 2014; Di Ruscio et al., 2013; Gao et al., 2020; Guo et al., 2019; Merry et al., 2015; Mohammad et al., 2010; O'Leary et al., 2017; Sun et al., 2016; Wang et al., 2015). To test if DNA methylation levels have changed in the KOs, we carried out immunofluorescence measurements using anti-5-methyl cytosine antibody (Figures 2A, S3A, Tables S2 and S3). Surprisingly, in KO lines, the 5-methyl cytosine signal was considerably weaker as compared with WT cells, indicating genomic DNA was hypomethylated (Figures 2A and S3A).

A potential explanation for hypomethylation of genomic DNA in *CCDC26* KO lines could be reduced levels of DNA methyltransferase proteins. However, immunoblotting in the *CCDC26* knockouts, showed no significant changes in the levels of the three DNA methyltransferase proteins, DNMT3a, DNMT3b, and DNMT1 (Figures 2B and S3B). Therefore, we speculated that DNA-binding capacity or the enzymatic activity of a DNA methyltransferase might have changed in the absence of *CCDC26*. To detect changes in the association of DNMTs with DNA, we performed anti-DNMT immunofluorescence. We observed that, in KOs, the subcellular localization of DNMT1 is predominantly cytosolic in contrast to WT where DNMT1 is, as expected, localized in the nucleus (Figure 2C). This was supported by immunoblotting measurements using anti-DNMT1 antibody on nuclear and cytosolic fractions of KOs as compared with WT (Figure 2D). However, mis-localization was not observed in case of DNMT3a and DNMT3b or other nuclear proteins such as HDAC2 (Figures S3C and S3D).

Genes repressed by DNMT1 are upregulated in KO cells

We further hypothesized that if DNMT1 protein mis-localizes in the cytosol, then DNMT1 would be unable to carry out its primary function of methylating genomic DNA in the nucleus. Consequently, these cells should behave similarly to cells lacking DNMT1. To confirm this, we investigated expression levels of a selection of seven genes, previously shown to be significantly impacted by DNMT1 and methylation levels in myeloid cells (Figure 3A). These were protein tyrosine phosphatase non-receptor type 6 (*PTPN6*) (Li et al., 2017; Wang et al., 2017), cyclin-dependent kinase inhibitor 1A (*CDKN1A*) (Milutinovic et al., 2004; Schmelz et al., 2005), cyclin-dependent kinase inhibitor 2B (*CDKN2B*) (Herman et al., 1996; Yu et al., 2013), *CD9* (Kim et al., 2012), *VAV1* (Fernandez-Zapico et al., 2005; Ilan and Katzav, 2012), and *JUNB* (Fiskus et al., 2009; Yang et al., 2003), all of which have previously demonstrated upregulation in response to DNMT1 downregulation or DNA hypomethylation. We also measured levels of *IGF1*, as it has previously been reported that *IGF1* is repressed as a result of DNMT1 inhibition (Pastural et al., 2007). qRT-PCRs demonstrated that out of seven genes we tested, five (*PTPN6*, *CDKN1A*, *CDKN2B*, *CD9*, and *VAV1*) were significantly upregulated in both KO cell lines as reported in past studies on DNMT1 KD or inhibition. *JUNB*, albeit not significantly, also demonstrated upregulation. As expected, *IGF1* was significantly downregulated in both KO cell lines. This result demonstrates that gene expression changes in *CCDC26* KO cells are very similar to cells in which DNMT1 has been knocked down or inhibited. Presumably this is due to the unavailability of DNMT1 in the *CCDC26* KOs, given its predominantly cytoplasmic localization in these cells.

To confirm if these genes were upregulated as a result of DNA methylation changes at their promoters, we measured DNA methylation levels at the promoters of *PTPN6*, *VAV1*, *CD9*, and *CDKN1A* genes that were significantly upregulated in *CCDC26* KOs as compared with WT. DNA methylation levels were measured

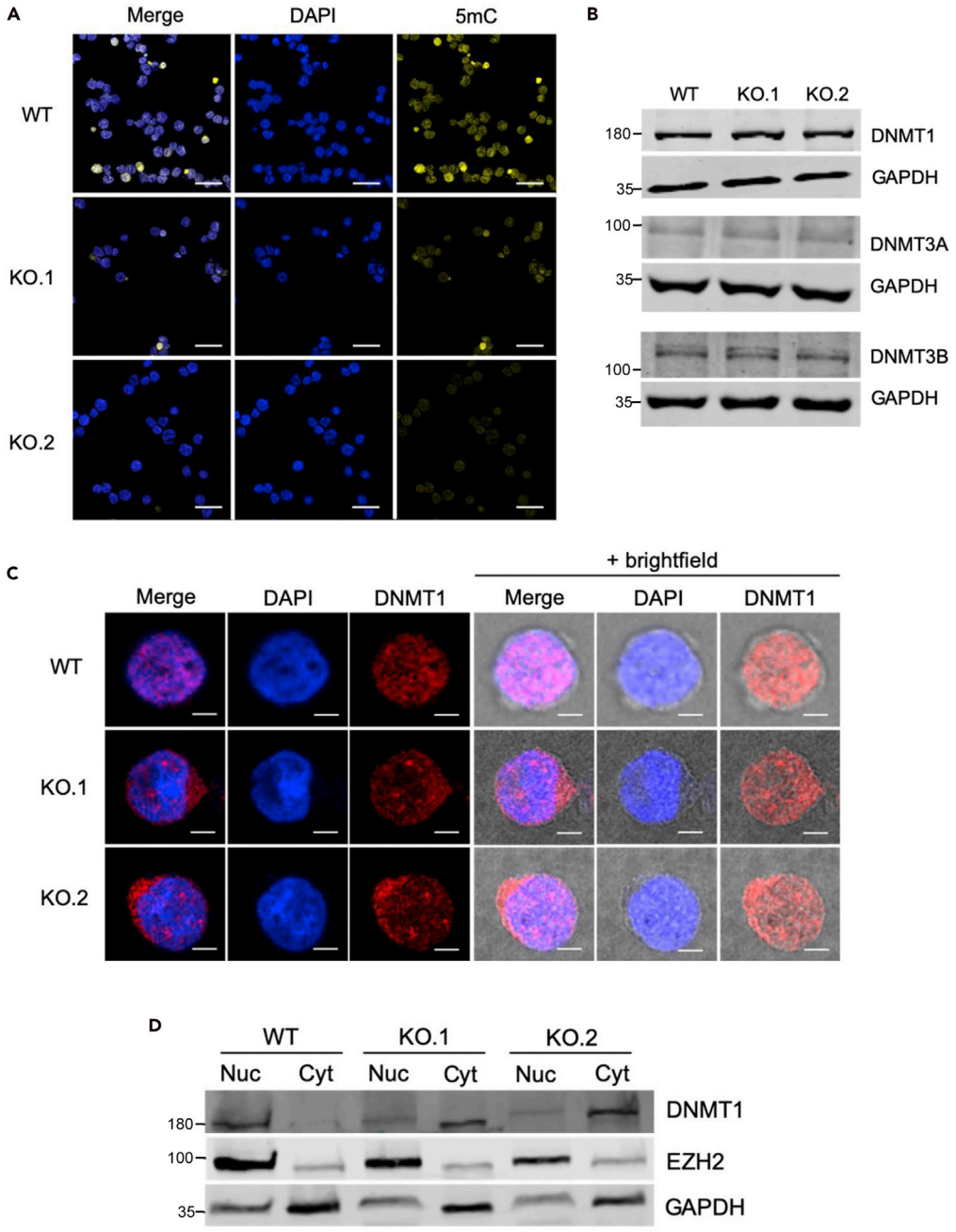

Figure 2. *CCDC26* knockout results in mis-localization of DNMT1 in the cytosol and global DNA hypomethylation

(A) Confocal images demonstrating the results of anti-5mC immunofluorescence. WT, KO.1, and KO.2 cells were stained with DAPI nuclear stain (blue) and anti-5mC antibody (yellow). Reduced levels of 5mC fluorescence are observed in both KO cell lines. Scale bar, 50 um.

(B) Total protein levels of DNMT1, DNMT3a, and DNMT3b measured relative to GAPDH by immunoblotting are unchanged in WT and *CCDC26* KO cells.

(C) Confocal images demonstrating the results of anti-DNMT1 immunofluorescence. WT, KO.1, and KO.2 cells were stained with DAPI nuclear stain (blue) and anti-DNMT1 antibody (red). The outline of the cell membrane can be seen with the addition of the brightfield lens in the right-hand panels. DNMT1 is nuclear in WT cells and is largely cytosolic in the KO cells. Scale bar, 5 um.

(D) Immunoblotting for DNMT1 on nuclear and cytosolic protein fractions shows a shift in the subcellular localization of DNMT1. DNMT1 is almost exclusively nuclear in the WT cells but appears both nuclear and cytosolic in *CCDC26* KO cells. EZH2 and GAPDH are used as nuclear and cytosolic markers, respectively (nuc = nuclear protein fraction; cyt = cytosolic protein fraction).

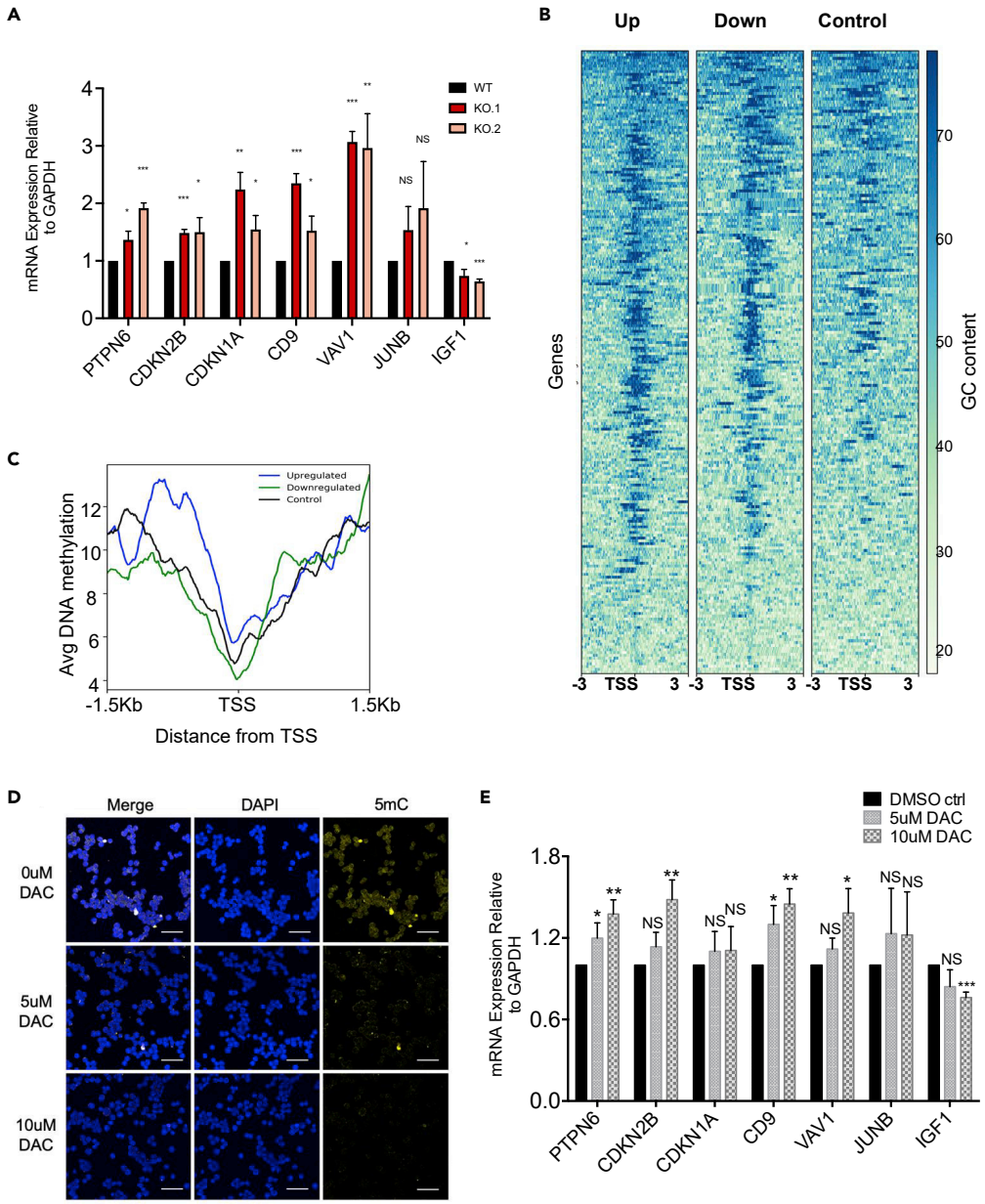

Figure 3. DNMT1 and methylation-regulated genes show expression changes in *CCDC26* KO cells

(A) A plot showing expression levels of various genes whose expression has previously been shown to be impacted by DNMT1 depletion or DNA hypomethylation in myeloid leukemia. Levels are measured relative to GAPDH in WT K562, KO.1, and KO.2 cells by qRT-PCR. Values represent the mean ± standard deviation. *p < 0.05; **p < 0.01; ***p < 0.001; NS = Not significant (unpaired, two-tailed *t* test).

(B and C) (B) Heatmaps showing GC distribution around of Transcription Start Sites (TSS) of 2-fold downregulated and upregulated genes in KO as well as same number of randomly selected control set of genes. (C) Metagene plots of average enrichment of DNA methylation K562 cells at 2-fold downregulated genes (blue) as compared with upregulated genes (green) in JARID2 KO cells and random set of genes as control (black). The plots are centered on TSS of genes, and distance from TSS is indicated on the x axes.

(D) Confocal images demonstrating the results of anti-5mC immunofluorescence on cells treated with either 0uM, 5uM, or 10uM DNMT1 inhibitor DAC. Cells were stained with DAPI nuclear stain (blue) and anti-5mC antibody (yellow). Reduced levels of 5mC fluorescence are observed in cells treated with 5uM and 10uM DAC. Scale bar, 50 um.

(E) A plot showing expression levels of various genes (as in A) whose expression has previously been shown to be impacted by DNMT1 depletion or DNA hypomethylation in myeloid leukemia. Levels are measured relative to GAPDH in cells treated with 0-uM, 5-uM, and 10-uM DNMT1 inhibitor DAC. Values represent the mean ± standard deviation. *p < 0.05; **p < 0.01; ***p < 0.001; NS = Not significant (unpaired, two-tailed *t* test).

using bisulfite conversion and followed by a pyrosequencing assay. We observed that, with the exception of *CDKN1A*, promoter methylation was reduced at the tested genes in both KOs (Tables S4 and S5 and Figure S4A).

In order to verify this at the genomic level, using RNA-seq we measured genome-wide changes in gene expression. RNA-seq analysis showed that, in total, 287 genes showed more than 2-fold changes in RNA levels in both KO lines. Among these, 146 were upregulated and 141 were downregulated. It was previously shown that DNA methylation of CpG rich promoters leads to transcriptional repression (Kass et al., 1997; Li et al., 1993; Siegfried et al., 1999; Venolia and Gartler, 1983; Walsh et al., 1998). If gene expression changes in *CCDC26* KO are due to mis-localization of DNMT1, promoter methylation-mediated repression of genes should be relieved in these cells. In other words, promoters of the genes upregulated in the KOs, should be GC-rich and should show a higher level of DNA methylation in WT cells. In order to verify this, we plotted GC density at differentially expressed genes against a random set of genes (Figure 3B). We observed that both up- and downregulated genes showed a much higher density of GC nucleotides compared with the control set of genes. In addition, we utilized previously published genome-wide DNA methylation levels in K562 cells to verify if the promoters of affected genes are methylated. As suspected, genes upregulated in KO cells show a much higher level of DNA methylation in K562 cells (Figure 3C), supporting the idea that gene expression changes we see in the KOs are due to changes in DNA methylation levels imposed by mis-localization of DNMT1 in the cytoplasm.

In order to further confirm that genes affected in the KO are regulated by DNMT1, we treated K562 cells with DNMT1 inhibitor, 5-aza-2′-deoxycytidine, also known as decitabine (DAC). DAC is a DNMT1 inhibitor that functions by covalently trapping DNMT1 to the DNA, thereby rendering it non-functional (Stresemann and Lyko, 2008). K562 WT cells were grown in the presence 0uM, 5uM, and 10uM DAC for 48 h. Treatment with both 5uM and 10uM DAC concentrations significantly reduced global 5mC levels (Figure 3D). DAC has also been shown to cause reductions in DNMT1 levels by inducing its proteasomal degradation (Ghoshal et al., 2005, 2018; Patel et al., 2010). Western blotting for DNMT1 also demonstrated decreased protein levels (Figure S4B).

Following confirmation of DNMT1 inhibition and global hypomethylation by DAC (Figure 3D), we next examined whether this elicited similar effects to that seen in *CCDC26* KO. Similar to the KOs, γ-H2AX immunofluorescence increased upon DNMT1 inhibition, indicating an increase in DNA damage in cells treated with both 5uM and 10uM DAC for 48 h (Figure S4C). Significantly, qRT-PCRs for DNMT1-regulated genes (Figure 3A) showed similar patterns of expression after DAC treatment as upon *CCDC26* KO (Figure 3E). Importantly, changes in gene expression were more pronounced in cells treated with 10uM DAC as compared with 5uM DAC (Figure 3E). These results support that reduction in DNMT1 can lead to DNA hypomethylation and subsequently DNA damage.

Apoptosis and DNA damage are a consequence of DNMT1 mis-localization

We next sought to establish the sequence of events that results in DNMT1 mis-localizing to the cytosol and DNA hypomethylation in *CCDC26* KO cells. In order to fully understand the functional mechanism of *CCDC26*, it is important to examine whether cytosolic localization of DNMT1 is a consequence of DNA damage and apoptosis.

To further confirm that DNMT1 mis-localization is a result of *CCDC26* KO and not a consequence of DNA damage, it was critical to establish that this type of movement of DNMT1 is not a general response to DNA damage and apoptosis. To investigate this, DNA damage was induced in WT cells using cisplatin. Cisplatin is a platinum-based drug that forms bonds with, and ultimately crosslinks, bases within and between DNA strands. This can distort the double helix, interfere with both DNA replication and transcription, and consequently induce DNA damage and apoptosis (Goodsell, 2006). To begin, the amount of cisplatin and treatment time required to induce DNA damage but prior to complete cell death was optimized (Figure S5A). Microscopic observations demonstrated that after 24 h of cisplatin treatment, cells treated with 5uM or 10uM of the drug still appeared viable. DNA damage was also confirmed in the cells treated with 5uM and 10uM cisplatin by monitoring γ-H2AX foci using immunofluorescence (Figure S5B).

To assess DNMT1 localization in DNA-damage-induced cells, DNMT1 immunofluorescence was performed on cisplatin-treated cells. This experiment exhibited no significant differences between 0uM control cells and the drug-treated cells. Similar to WT K562 cells, in cisplatin-treated cells, DNMT1 appeared primarily nuclear, demonstrating a diffused pattern of distribution throughout (Figure 4A). Accordingly,

there was also no substantial change in the levels of 5mC immunofluorescence between control and cisplatin-treated cells (Figure 4B). This suggests that DNMT1 mis-localization in cytoplasm is not a general consequence of DNA damage. As further confirmation, the expression levels of genes that are up- or down-regulated in response to *CCDC26* KO and DNMT1 inhibition (as shown in Figure 3A) were also tested in cisplatin-treated cells. Some genes (*IGF1* and *CDKN1A*) demonstrated similar changes in expression patterns in response to cisplatin as they did in response to DNMT inhibition and *CCDC26* KO. However, for majority of genes, expression was either not significantly altered or they demonstrated an opposite change in expression (Figure S5C). This suggests that the expression changes seen in the KOs are response to DNMT1 mis-localization and DNA hypomethylation but not a consequence of DNA damage. Interestingly, *CDKN1A* gene whose promoter methylation was not affected by *CCDC26* KO (Figure S4A) was the only gene that was significantly upregulated in cisplatin-treated cells, indicating that changes in *CDKN1A* expression were in response to DNA damage downstream of DNA hypomethylation.

CCDC26 is a nuclear lincRNA and interacts with DNMT1

To further investigate the relationship between *CCDC26* and DNMT1, we investigated the possibility that *CCDC26* interacts with DNMT1, thereby influencing its cellular localization. We first endeavored to find out the cellular localization of *CCDC26* RNA. A large proportion of lncRNAs that have shown a predominantly nuclear localization are either associated with chromatin or enriched in nuclear sub-compartments and organelles (Clemson et al., 2009; Hutchinson et al., 2007; Werner and Ruthenburg, 2015). The subcellular localization of a lncRNA can give a clue to its functional mechanism. Previous results showed that *CCDC26* might be marginally enriched in nucleus (Hirano et al., 2015). In this previous publication, all *CCDC26* isoforms were not tested for their localization. It is possible that only selected isoforms are nuclear, thus influencing *CCDC26* function. To understand the localization, we measured the levels of all four *CCDC26* isoforms using qRT-PCRs in nuclear and cytosolic RNA fractions (Figure 5A). snoRNA U105 and GAPDH were used as gene markers to assess the quality of nuclear and cytosolic fractions, respectively (Figure S6A). Actin was used as a housekeeping control gene against which *CCDC26* expression could be measured, given its similar levels in both the nucleus and cytosol (Figure S6B). Consistent with previous publication (Hirano et al., 2015), we found that all *CCDC26* isoforms were much more enriched in the nucleus as compared with the cytosol (Figure 5A). To determine the location of *CCDC26* in the nucleus, we also performed fluorescence *in situ* hybridization (RNA-FISH) on WT and KO cells. A fluorescently labeled probe specific to exon 6 of *CCDC26* was generated and used for RNA FISH, followed by analysis using confocal microscopy. Interestingly, microscopic images (Figure 5B) showed that *CCDC26* is predominantly located within the nucleus, demonstrating an enrichment at the periphery of the nucleus. The absence of fluorescent *CCDC26* signal in the KO cells indicated that the signal was specific (Figure 5B).

It is important to establish whether DNMT1 mis-localization could be due to a direct interaction between *CCDC26* and DNMT1 or an indirect effect of *CCDC26* knockout. DNMT1 has previously been shown to bind and undergo regulation by multiple lncRNAs (Bao et al., 2015; Chalei et al., 2014; Di Ruscio et al., 2013; Gao et al., 2020; Guo et al., 2019; Merry et al., 2015; Mohammad et al., 2010; O'Leary et al., 2017; Sun et al., 2016; Wang et al., 2015). It has also been suggested that DNMT1 has higher affinity for RNA than DNA (Di Ruscio et al., 2013; Merry et al., 2015). Nuclear localization of *CCDC26* points to a possibility that this lincRNA might also interact with DNMT1 in the nucleus. To further confirm this, we performed DNMT1 RNA immunoprecipitation (RIP) using anti-DNMT1 antibody (Figure 5C). An anti-IgG antibody was used to produce a control sample. The protein-bound-RNA pulled down with anti-DNMT1 and anti-IgG antibodies was used to perform qRT-PCRs with primers specific to *CCDC26*, and the RNA levels were measured relative to the input. Anti-DNMT1 pulled-down RNA showed approximately three times more enrichment of *CCDC26* compared with the IgG control (Figure 5C). Moreover, enrichment of *CCDC26* in the RIP assay is comparable to another long non-coding RNA, *KCNQ1OT1* (Figure 5C), which was previously shown to interact with DNMT1(Mohammad et al., 2010). This raises a possibility that *CCDC26* directly or indirectly interacts with DNMT1. However, the exact nature of *CCDC26* and DNMT1 interaction needs to be confirmed with a more detailed investigation.

However, we can get additional support for this interaction by analyzing previously studied protein-RNA interactions that have been studied using RIP or variations of this method (Bai et al., 2019; Di Ruscio et al., 2013; Hendrickson et al., 2016; Hui et al., 2019; Xu et al., 2019). At least two datasets exploring DNMT1-RNA interactions in myeloid cells have been published (Di Ruscio et al., 2013; Hendrickson et al., 2016). We first adopted a bioinformatics approach where we re-mapped previously published RIP-seq datasets to the *CCDC26* locus. The first dataset that we analyzed was generated using another myeloid line, HL60 (Di Ruscio et al., 2013). These data

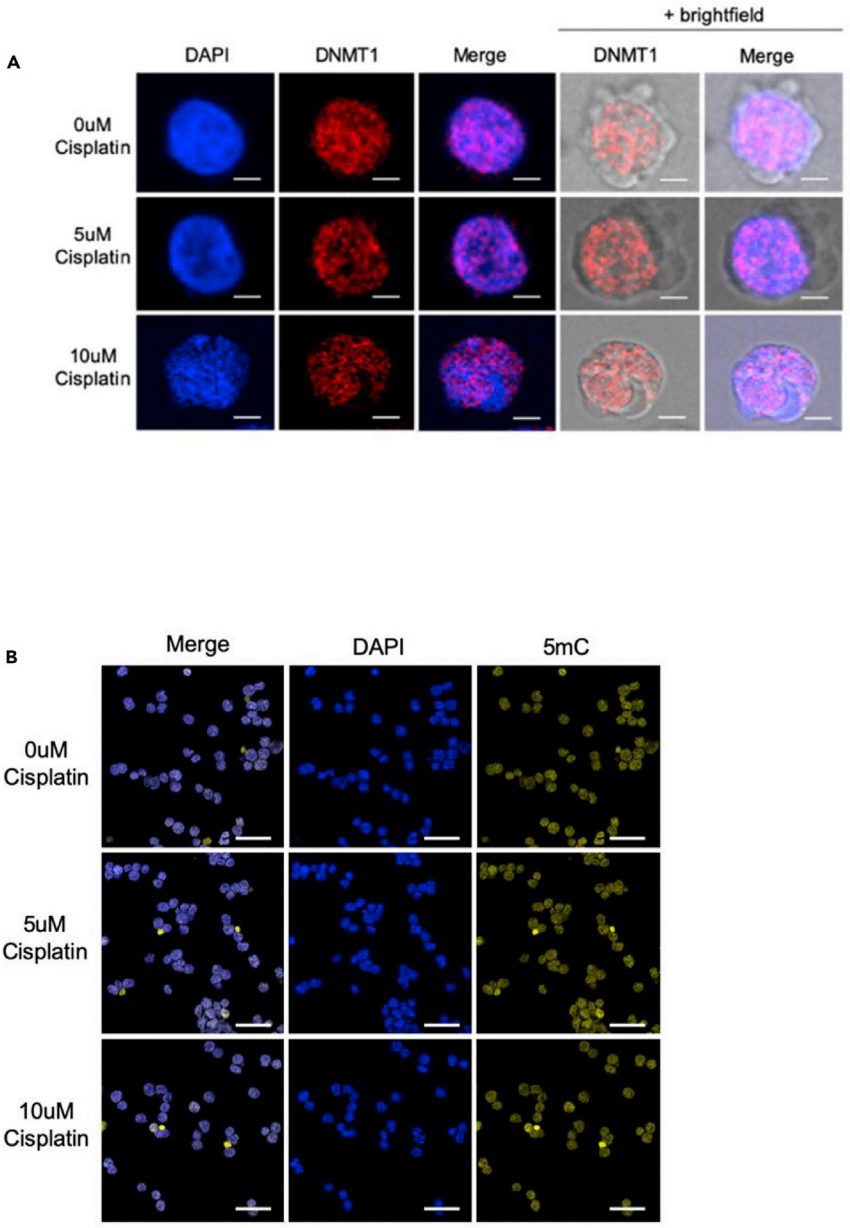

Figure 4. Cisplatin-induced DNA damage does not result in subcellular mis-localization of DNMT1

(A) Confocal images demonstrating the results of anti-DNMT1 immunofluorescence. Cells treated with 0 uM, 5 uM, and 10 uM cisplatin were stained with DAPI nuclear stain (blue) and anti-DNMT1 antibody (red). The outline of the cell membrane can be seen with the addition of the brightfield lens in the right-hand panels. DNMT1 appears nuclear in cells treated with different cisplatin concentrations. Scale bar, 5 um.

(B) Confocal images demonstrating the results of anti-5mC immunofluorescence on cells treated with either 0 uM, 5 uM, or 10 uM cisplatin. Cells were stained with DAPI nuclear stain (blue) and anti-5mC antibody (yellow). Similar levels of 5mC fluorescence are observed in cells treated with different cisplatin concentrations. Scale bar, 50 um.

were generated by first pulling down cellular RNAs that bind to DNMT1 using anti-DNMT1 antibody and then sequencing and mapping these RNAs to the human genome. These data showed that *CCDC26* is highly enriched in DNMT1-RIP assays when compared with an IgG RIP control (Figure S6C). Furthermore, analysis of another dataset, produced by a variation of the RIP method, formaldehyde-RIP-seq (fRIP-seq), also showed high enrichment of *CCDC26* in DNMT1-bound RNAs in K562 cells (Hendrickson et al., 2016), further confirming an interaction between DNMT1-*CCDC26* (Figure S6D).

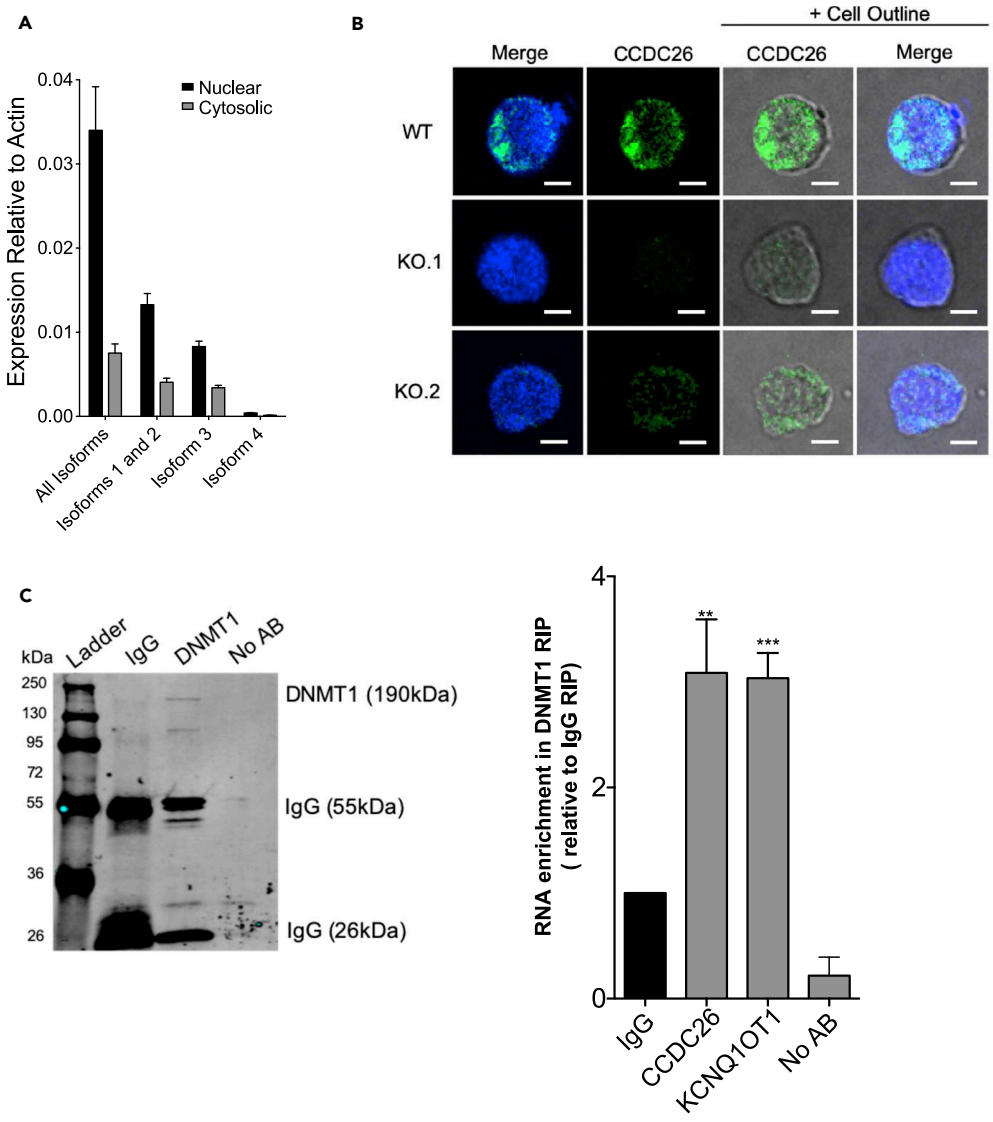

Figure 5. *CCDC26* is a nuclear lincRNA and interacts with DNMT1

(A) A plot showing the levels of different *CCDC26* isoforms, relative to Actin, in nuclear and cytosolic fractions of WT K562 cells, measured using qRT-PCR. Greater presence of all *CCDC26* isoforms was found in the nuclear fraction. Error bars represent the mean ± standard deviation.

(B) Confocal images demonstrating the results of RNA FISH using a *CCDC26*-specific fluorescent probe. WT, KO.1, and KO.2 cells were stained with DAPI nuclear stain (blue) and a *CCDC26* probe (green). The outline of the cell membrane can be seen with the addition of the brightfield lens in the right-hand panels. *CCDC26* is primarily localized in the nucleus of the cell, specifically at the nuclear periphery. Scale bar, 5 um.

(C) Protein-RNA complexes pulled down with either anti-IgG, anti-DNMT1, or no antibody were immunoblotted with anti-DNMT1, to ensure that the DNMT1 protein was correctly pulled down for RNA immunoprecipitation. RNA pulled-down in each IP was purified, converted to cDNA, and subjected to qRT-PCR with *CCDC26 and KCNQ1OT1* primers, to determine how much RNA was pulled down relative to the input in each instance. Values represent the mean ± standard deviation. *p < 0.05; **p < 0.01; ***p < 0.001; NS = Not significant (unpaired, two-tailed t test).

DISCUSSION

In the last three decades, following the development of whole-genome technologies, lncRNAs have gained importance (Derrien et al., 2012; Hangauer et al., 2013; Iyer et al., 2015; Okazaki et al., 2002), with many examples demonstrating their role in transcription regulation.

Here we have performed functional analysis of lincRNA, *CCDC26* and demonstrated its importance in regulating global DNA methylation. Our data show that, in the absence of *CCDC26*, the genome is hypomethylated, which leads to increase in apoptosis and DNA damage and cell growth inhibition. In the past, non-coding RNAs have been shown to impact DNA methylation levels through transcriptional and post-transcriptional regulation of DNMT genes (Chen et al., 2015; Cheng et al., 2018; Di Ruscio et al., 2013; Merry et al., 2015; Mohammad et al., 2010; Wang et al., 2018). However, DNMT expression levels were unchanged in *CCDC26* KOs, indicating that the mechanism behind the observed DNA hypomethylation is different. Strikingly, in the absence of lincRNA *CCDC26*, a large proportion of DNMT1 protein is mis-localized in the cytosol. In KO cells, the mis-localization of DNMT1 in cytoplasm is most likely responsible for the observed hypomethylated state of the genome and cell death. This connection between *CCDC26* and DNMT1 can provide the missing link between frequent mutations in *CCDC26* locus and leukemia. Deletion of DNMT1 is shown to prevent MLL-AF9 leukemia. In addition, it has been reported that the absence of DNMT1 induces apoptosis in hematopoietic stem cells. This is similar to what we observe in this study when *CCDC26* is removed. In corollary, direct or indirect role of *CCDC26* in retaining DNMT1 in nucleus and also maintaining cell proliferation can explain why *CCDC26* is often upregulated in AML (Duployez et al., 2018; Izadifard et al., 2018; Kuhn et al., 2012; Radtke et al., 2009).

LncRNA-mediated regulation of cellular localization, although not reported in case of DNMT1, has been previously reported in case of other proteins. In some instances, this has been shown to occur via a direct interaction; for example, lncRNA *TP53TG1* binds the transcription factor, YBX1, thereby preventing its nuclear trafficking (Diaz-Lagares et al., 2016). In other instances, this can also occur via an indirect effect; an interaction between lncRNA *CRYBG3* and actin for example is sufficient to prevent translocation of myelin and lymphocyte protein (MAL) into the nucleus (Pei et al., 2018). Similarly, NF_kB-interacting LncRNA (*NKILA*) binds and prevents phosphorylation of the inhibitory IκB subunit. This blocks its degradation, which subsequently prevents the active p65 subunit of NF_kB from re-localizing from the cytosol to the nucleus (Liu et al., 2015). However, we did not observe any changes in DNMT1 stability upon *CCDC26* KO (Figure S7). Moreover, we demonstrate an interaction between DNMT1 and *CCDC26*, suggesting that this lincRNA might play a direct or indirect role in localizing DNMT1 in the nucleus.

Numerous DNMT1-interacting lncRNAs have been identified previously (Bao et al., 2015; Chalei et al., 2014; Di Ruscio et al., 2013; Gao et al., 2020; Guo et al., 2019; Merry et al., 2015; Mohammad et al., 2010; O'Leary et al., 2017; Sun et al., 2016; Wang et al., 2015); however, these largely demonstrate effects on DNA methylation at localized genes or regions, as opposed to the global effect observed here. In addition, lincRNA-mediated DNMT1 localization has not been reported before. Based on these results, we provide a model (Figure 6) suggesting that lincRNAs, in this case *CCDC26*, can regulate sub-cellular localization of DNMT1 via direct or indirect interaction in the nucleus. This provides a means of regulating global genomic DNA methylation, and disruption of the lincRNA can result in hypomethylation and apoptosis.

A major question that remains in this instance is how *CCDC26* orchestrates nuclear localization of DNMT1 and the mechanism that causes its cytosolic mis-localization in the absence of *CCDC26*. Independent of lincRNAs, in rare circumstances, DNMT1 localization in the cytoplasm has been demonstrated and can provide clues regarding the mechanism behind lincRNA-mediated DNMT1 localization. Arguably the best studied of these instances is during preimplantation in early development. An oocyte-specific form of DNMT1, DNMT1o, demonstrates a preferential localization within the cytosol during preimplantation development. DNMT1o lacks 118 amino acids at the N-terminus compared with somatic DNMT1. It has been postulated that an alternative, extended region of the N-terminus is critical, and complex folding of this area likely plays a large part in overriding the NLS. This is required for demethylation of the embryonic genome, upon which lineage specific methylation patterns are established (Cardoso and Leonhardt, 1999). In instances other than during embryonic development, cytosolic localization of DNMT1 tends to be aberrant; for example, it has been associated with several neurological disorders including hereditary sensory and autonomic neuropathy type 1E (HSAN1E) (Baets et al., 2015), Alzheimer disease (Mastroeni et al., 2013) and Parkinson disease (Desplats et al., 2011), as well as cancer tumorigenesis (Arzenani et al., 2011; Hodge et al., 2007). The reasons behind aberrant cytosolic localization of DNMT1 is not entirely clear. Various mechanisms including changes to post-translational modifications of DNMT1 (Hodge et al., 2007), HDAC inhibition (Arzenani et al., 2011), mutations within the RFTS domain (Baets et al., 2015), and disruption to nucleo-cytoplasmic transport systems across the nuclear membrane (Mastroeni et al., 2013) have been reported. Given that previous reports of cytosolic DNMT1 have often involved the N-terminal domain of DNMT1 (Baets et al., 2015; Cardoso and Leonhardt, 1999; Hodge et al., 2007), where the NLS

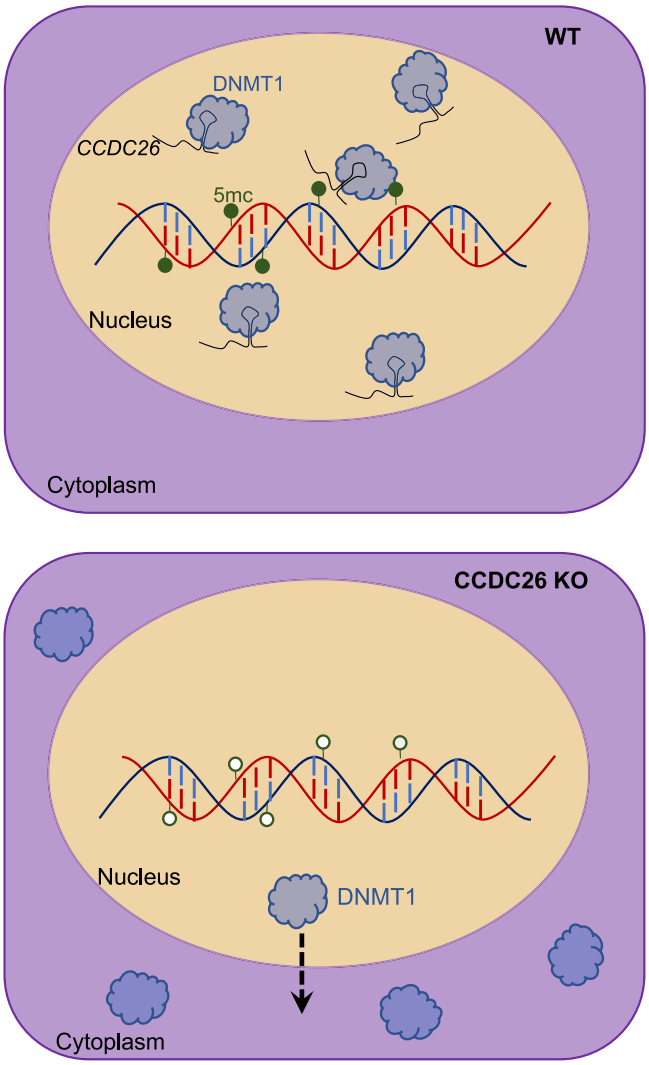

Figure 6. Model for *CCDC26*-mediated DNMT1 regulation

In WT K562 cells, DNMT1 directly or indirectly interacts with *CCDC26*. DNMT1 is almost exclusively localized in the nucleus where it maintains DNA methylation patterns as cells replicate. In the absence of *CCDC26*, DNMT1 is re-localized to the cytoplasm and cells become hypomethylated.

resides, it can be speculated that this region of the protein may be affected by *CCDC26*, possibly through lincRNA-mediated post-translational modifications or protein folding.

Limitations of the study

Although our study shows that *CCDC26* influences DNMT1 localization, to gain further insights into how *CCDC26* functions, we will have to address a number of questions and will need to carry out a more detailed investigation. Our RIP assay indicates that *CCDC26* is similarly enriched in DNMT1 pulldown as other ncRNAs that are previously reported to bind to DNMT1. However, we will need to confirm if this is a direct or indirect interaction. We can speculate that the interaction of *CCDC26* with DNMT1 leads to changes in the configuration of DNMT1's nuclear localization domain that are needed for retaining DNMT1 in the nucleus. RNA-binding domain of DNMT1 is previously mapped, and it overlaps its C-terminal enzymatic domain (Di Ruscio et al., 2013). We will need to verify that *CCDC26* binds to the same domain, and also, we will need to investigate the relationship between *CCDC26* binding domain and nuclear localization domain of DNMT1. If *CCDC26* and DNMT1 interact *in vivo* we expect them to colocalize in the cell. Our microscopy observations show that both DNMT1 and *CCDC26* are nuclear. But, in addition, we have also observed that *CCDC26* also accumulates

in the nuclear periphery. We have not studied the significance of accumulation of *CCDC26* in the nuclear periphery. However, our observation that *CCDC26* knockout does not affect localization of other nuclear proteins such as EZH2 and HDAC2 shows that the role of *CCDC26* is specific and it does not affect all nuclear proteins. Lastly, it is important to see if DNMT1 mis-localization is reversible and if re-introducing *CCDC26* in the cells will re-localize DNMT1 in the nucleus. Currently, many of these questions are out of scope of this study but will need to be addressed in the future.

In summary, even though detailed molecular mechanism behind *CCDC26*-mediated DNMT1 localization still remains to be investigated, our study provides an insight into the role of *CCDC26* in cancer as well as a novel lincRNA mechanism of DNMT1 regulation.

Resource availability

Lead contact

Further information and requests for resources and reagents should be directed to and will be fulfilled by the lead contact, Aditi Kanhere (a.kanhere@liverpool.ac.uk).

Materials availability

This study did not generate new unique reagents.

Data and code availability

The accession number for the RNA-sequencing data generated and reported in this paper is GEO: GSE105029.

METHODS

All methods can be found in the accompanying transparent methods supplemental file.

SUPPLEMENTAL INFORMATION

Supplemental information can be found online at https://doi.org/10.1016/j.isci.2021.102273.

ACKNOWLEDGMENTS

We thank Dr J Woolley, Dr M Winch, and Dr E Petermann for useful discussions. We are also grateful to Dr Alessandro Di Maio for help with microscopy data analysis. During the course of study, AK was funded by SSfH fellowship from University of Birmingham. RJ was supported by BBSRC MIBTP fellowship. SW was supported by MRC Doctoral Training Program and University of Birmingham.

AUTHOR CONTRIBUTIONS

AK conceived the study. RH and AK wrote the manuscript. RH, SW, JH, CW, TL, and AK designed and carried out the experiments.

DECLARATION OF INTERESTS

Authors declare no competing financial interest.

Received: June 16, 2020
Revised: December 21, 2020
Accepted: March 2, 2021
Published: April 23, 2021

REFERENCES

Alvarez-Ponce, D., Torres-Sanchez, M., Feyertag, F., Kulkarni, A., and Nappi, T. (2018). Molecular evolution of DNMT1 in vertebrates: duplications in marsupials followed by positive selection. PLoS One *13*, e0195162.

Arzenani, M.K., Zade, A.E., Ming, Y., Vijverberg, S.J., Zhang, Z., Khan, Z., Sadique, S., Kallenbach, L., Hu, L., Vukojevic, V., et al. (2011). Genomic DNA hypomethylation by histone deacetylase inhibition implicates DNMT1 nuclear dynamics. Mol. Cell Biol. *31*, 4119–4128.

Baets, J., Duan, X., Wu, Y., Smith, G., Seeley, W.W., Mademan, I., McGrath, N.M., Beadell, N.C., Khoury, J., Botuyan, M.V., et al. (2015). Defects of mutant DNMT1 are linked to a spectrum of neurological disorders. Brain *138*, 845–861.

Bai, Y., Wang, W., Zhang, Y., Zhang, F., and Zhang, H. (2019). lncRNA MIAT suppression alleviates corneal angiogenesis through regulating miR-1246/ACE. Cell Cycle *18*, 661–669.

Bao, X., Wu, H., Zhu, X., Guo, X., Hutchins, A.P., Luo, Z., Song, H., Chen, Y., Lai, K., Yin, M., et al. (2015). The p53-induced lincRNA-p21 derails somatic cell reprogramming by sustaining H3K9me3 and CpG methylation at pluripotency gene promoters. Cell Res. *25*, 80–92.

Berghoff, E.G., Clark, M.F., Chen, S., Cajigas, I., Leib, D.E., and Kohtz, J.D. (2013). Evf2 (Dlx6as) lncRNA regulates ultraconserved enhancer methylation and the differential transcriptional control of adjacent genes. Development *140*, 4407–4416.

Berkyurek, A.C., Suetake, I., Arita, K., Takeshita, K., Nakagawa, A., Shirakawa, M., and Tajima, S. (2014). The DNA methyltransferase Dnmt1 directly interacts with the SET and RING finger-associated (SRA) domain of the multifunctional protein Uhrf1 to facilitate accession of the catalytic center to hemi-methylated DNA. J. Biol. Chem. *289*, 379–386.

Bostick, M., Kim, J.K., Esteve, P.O., Clark, A., Pradhan, S., and Jacobsen, S.E. (2007). UHRF1 plays a role in maintaining DNA methylation in mammalian cells. Science *317*, 1760–1764.

Bronner, C., Alhosin, M., Hamiche, A., and Mousli, M. (2019). Coordinated dialogue between UHRF1 and DNMT1 to ensure faithful inheritance of methylated DNA patterns. Genes (Basel) *10*, 65.

Cardoso, M.C., and Leonhardt, H. (1999). DNA methyltransferase is actively retained in the cytoplasm during early development. J. Cell Biol. *147*, 25–32.

Chalei, V., Sansom, S.N., Kong, L., Lee, S., Montiel, J.F., Vance, K.W., and Ponting, C.P. (2014). The long non-coding RNA Dali is an epigenetic regulator of neural differentiation. Elife *3*, e04530.

Chen, Z., Liu, S., Tian, L., Wu, M., Ai, F., Tang, W., Zhao, L., Ding, J., Zhang, L., and Tang, A. (2015). miR-124 and miR-506 inhibit colorectal cancer progression by targeting DNMT3B and DNMT1. Oncotarget *6*, 38139–38150.

Cheng, D., Deng, J., Zhang, B., He, X., Meng, Z., Li, G., Ye, H., Zheng, S., Wei, L., Deng, X., et al. (2018). LncRNA HOTAIR epigenetically suppresses miR-122 expression in hepatocellular carcinoma via DNA methylation. EBioMedicine *36*, 159–170.

Clemson, C.M., Hutchinson, J.N., Sara, S.A., Ensminger, A.W., Fox, A.H., Chess, A., and Lawrence, J.B. (2009). An architectural role for a nuclear noncoding RNA: NEAT1 RNA is essential for the structure of paraspeckles. Mol. Cell *33*, 717–726.

Csankovszki, G., Nagy, A., and Jaenisch, R. (2001). Synergism of Xist RNA, DNA methylation, and histone hypoacetylation in maintaining X chromosome inactivation. J. Cell Biol. *153*, 773–784.

Daskalos, A., Nikolaidis, G., Xinarianos, G., Savvari, P., Cassidy, A., Zakopoulou, R., Kotsinas, A., Gorgoulis, V., Field, J.K., and Liloglou, T. (2009). Hypomethylation of retrotransposable elements correlates with genomic instability in non-small cell lung cancer. Int. J. Cancer *124*, 81–87.

Derrien, T., Johnson, R., Bussotti, G., Tanzer, A., Djebali, S., Tilgner, H., Guernec, G., Martin, D., Merkel, A., Knowles, D.G., et al. (2012). The GENCODE v7 catalog of human long noncoding RNAs: analysis of their gene structure, evolution, and expression. Genome Res. *22*, 1775–1789.

Desplats, P., Spencer, B., Coffee, E., Patel, P., Michael, S., Patrick, C., Adame, A., Rockenstein, E., and Masliah, E. (2011). Alpha-synuclein sequesters Dnmt1 from the nucleus: a novel mechanism for epigenetic alterations in Lewy body diseases. J. Biol. Chem. *286*, 9031–9037.

Di Ruscio, A., Ebralidze, A.K., Benoukraf, T., Amabile, G., Goff, L.A., Terragni, J., Figueroa, M.E., De Figueiredo Pontes, L.L., Alberich-Jorda, M., Zhang, P., et al. (2013). DNMT1-interacting RNAs block gene-specific DNA methylation. Nature *503*, 371–376.

Diaz-Lagares, A., Crujeiras, A.B., Lopez-Serra, P., Soler, M., Setien, F., Goyal, A., Sandoval, J., Hashimoto, Y., Martinez-Cardus, A., Gomez, A., et al. (2016). Epigenetic inactivation of the p53-induced long noncoding RNA TP53 target 1 in human cancer. Proc. Natl. Acad. Sci. U S A *113*, E7535–E7544.

Doherty, A.S., Bartolomei, M.S., and Schultz, R.M. (2002). Regulation of stage-specific nuclear translocation of Dnmt1o during preimplantation mouse development. Dev. Biol. *242*, 255–266.

Duployez, N., Boudry-Labis, E., Roumier, C., Boissel, N., Petit, A., Geffroy, S., Helevaut, N., Celli-Lebras, K., Terre, C., Fenneteau, O., et al. (2018). SNP-array lesions in core binding factor acute myeloid leukemia. Oncotarget *9*, 6478–6489.

Eden, A., Gaudet, F., Waghmare, A., and Jaenisch, R. (2003). Chromosomal instability and tumors promoted by DNA hypomethylation. Science *300*, 455.

Esteve, P.O., Chin, H.G., Smallwood, A., Feehery, G.R., Gangisetty, O., Karpf, A.R., Carey, M.F., and Pradhan, S. (2006). Direct interaction between DNMT1 and G9a coordinates DNA and histone methylation during replication. Genes Dev. *20*, 3089–3103.

Fernandez-Zapico, M.E., Gonzalez-Paz, N.C., Weiss, E., Savoy, D.N., Molina, J.R., Fonseca, R., Smyrk, T.C., Chari, S.T., Urrutia, R., and Billadeau, D.D. (2005). Ectopic expression of VAV1 reveals an unexpected role in pancreatic cancer tumorigenesis. Cancer Cell *7*, 39–49.

Fiskus, W., Buckley, K., Rao, R., Mandawat, A., Yang, Y., Joshi, R., Wang, Y., Balusu, R., Chen, J., Koul, S., et al. (2009). Panobinostat treatment depletes EZH2 and DNMT1 levels and enhances decitabine mediated de-repression of JunB and loss of survival of human acute leukemia cells. Cancer Biol. Ther. *8*, 939–950.

Fuks, F., Hurd, P.J., Deplus, R., and Kouzarides, T. (2003). The DNA methyltransferases associate with HP1 and the SUV39H1 histone methyltransferase. Nucleic Acids Res. *31*, 2305–2312.

Gao, J., Dai, C., Yu, X., Yin, X.B., Liao, W.J., Huang, Y., and Zhou, F. (2020). Silencing of long non-coding RNA FOXD2-AS1 inhibits the progression of gallbladder cancer by mediating methylation-dependent induction of MLH1. Gene Therapy. https://doi.org/10.1038/s41434-020-00187-w.

Gaudet, F., Hodgson, J.G., Eden, A., Jackson-Grusby, L., Dausman, J., Gray, J.W., Leonhardt, H., and Jaenisch, R. (2003). Induction of tumors in mice by genomic hypomethylation. Science *300*, 489–492.

Ghoshal, K., Datta, J., Majumder, S., Bai, S., Kutay, H., Motiwala, T., and Jacob, S.T. (2005). 5-Aza-deoxycytidine induces selective degradation of DNA methyltransferase 1 by a proteasomal pathway that requires the KEN box, bromo-adjacent homology domain, and nuclear localization signal. Mol. Cell Biol. *25*, 4727–4741.

Ghoshal, K., Datta, J., Majumder, S., Bai, S., Kutay, H., Motiwala, T., and Jacob, S.T. (2018). Correction for Ghoshal et al., "5-Aza-Deoxycytidine Induces Selective Degradation of DNA Methyltransferase 1 by a Proteasomal Pathway That Requires the KEN Box, Bromo-Adjacent Homology Domain, and Nuclear Localization Signal". Mol. Cell Biol. *38*, e00539-17.

Goodsell, D.S. (2006). The molecular perspective: Cisplatin. Stem Cells *24*, 514–515.

Guo, X., Chen, Z., Zhao, L., Cheng, D., Song, W., and Zhang, X. (2019). Long non-coding RNA-HAGLR suppressed tumor growth of lung adenocarcinoma through epigenetically silencing E2F1. Exp. Cell Res. *382*, 111461.

Hangauer, M.J., Vaughn, I.W., and McManus, M.T. (2013). Pervasive transcription of the human genome produces thousands of previously unidentified long intergenic noncoding RNAs. PLoS Genet. *9*, e1003569.

Heller, G., Topakian, T., Altenberger, C., Cerny-Reiterer, S., Herndlhofer, S., Ziegler, B., Datlinger, P., Byrgazov, K., Bock, C., Mannhalter, C., et al. (2016). Next-generation sequencing identifies major DNA methylation changes during progression of Ph+ chronic myeloid leukemia. Leukemia *30*, 1861–1868.

Hendrickson, G., Kelley, D.R., Tenen, D., Bernstein, B., and Rinn, J.L. (2016). Widespread RNA binding by chromatin-associated proteins. Genome Biol. *17*, 28.

Herman, J.G., Jen, J., Merlo, A., and Baylin, S.B. (1996). Hypermethylation-associated inactivation indicates a tumor suppressor role for p15INK4B. Cancer Res. *56*, 722–727.

Hirano, T., Yoshikawa, R., Harada, H., Harada, Y., Ishida, A., and Yamazaki, T. (2015). Long noncoding RNA, CCDC26, controls myeloid leukemia cell growth through regulation of KIT expression. Mol. Cancer *14*, 90.

Hodge, D.R., Cho, E., Copeland, T.D., Guszczynski, T., Yang, E., Seth, A.K., and Farrar, W.L. (2007). IL-6 enhances the nuclear translocation of DNA cytosine-5-methyltransferase 1 (DNMT1) via phosphorylation of the nuclear localization sequence by the AKT kinase. Cancer Genomics Proteomics *4*, 387–398.

Hui, B., Ji, H., Xu, Y., Wang, J., Ma, Z., Zhang, C., Wang, K., and Zhou, Y. (2019). RREB1-induced upregulation of the lncRNA AGAP2-AS1 regulates the proliferation and migration of

pancreatic cancer partly through suppressing ANKRD1 and ANGPTL4. Cell Death Dis. *10*, 207.

Hutchinson, J.N., Ensminger, A.W., Clemson, C.M., Lynch, C.R., Lawrence, J.B., and Chess, A. (2007). A screen for nuclear transcripts identifies two linked noncoding RNAs associated with SC35 splicing domains. BMC Genomics *8*, 39.

Iida, T., Suetake, I., Tajima, S., Morioka, H., Ohta, S., Obuse, C., and Tsurimoto, T. (2002). PCNA clamp facilitates action of DNA cytosine methyltransferase 1 on hemimethylated DNA. Genes Cells *7*, 997–1007.

Ilan, L., and Katzav, S. (2012). Human Vav1 expression in hematopoietic and cancer cell lines is regulated by c-Myb and by CpG methylation. PLoS One *7*, e29939.

Imamura, T., Yamamoto, S., Ohgane, J., Hattori, N., Tanaka, S., and Shiota, K. (2004). Non-coding RNA directed DNA demethylation of Sphk1 CpG island. Biochem. Biophys. Res. Commun. *322*, 593–600.

Iyer, M.K., Niknafs, Y.S., Malik, R., Singhal, U., Sahu, A., Hosono, Y., Barrette, T.R., Prensner, J.R., Evans, J.R., Zhao, S., et al. (2015). The landscape of long noncoding RNAs in the human transcriptome. Nat. Genet. *47*, 199–208.

Izadifard, M., Pashaiefar, H., Yaghmaie, M., Montazeri, M., Sadraie, M., Momeny, M., Jalili, M., Ahmadvand, M., Ghaffari, S.H., Mohammadi, S., et al. (2018). Expression analysis of PVT1, CCDC26, and CCAT1 long noncoding RNAs in acute myeloid leukemia patients. Genet. Test Mol. Biomarkers *22*, 593–598.

Jaenisch, R., and Bird, A. (2003). Epigenetic regulation of gene expression: how the genome integrates intrinsic and environmental signals. Nat. Genet. *33* (*Suppl*), 245–254.

Jeffery, L., and Nakielny, S. (2004). Components of the DNA methylation system of chromatin control are RNA-binding proteins. J. Biol. Chem. *279*, 49479–49487.

Kass, S.U., Landsberger, N., and Wolffe, A.P. (1997). DNA methylation directs a time-dependent repression of transcription initiation. Curr. Biol. *7*, 157–165.

Kim, K.M., Small, D., and Scott, R.J. (2012). Gene expression profiling of human myeloid leukemic MV4-11 cells treated with 5-Aza-2′-deoxycytidine. J. Cancer Ther. *3*, 177–182.

Klein, C.J., Bird, T., Ertekin-Taner, N., Lincoln, S., Hjorth, R., Wu, Y., Kwok, J., Mer, G., Dyck, P.J., and Nicholson, G.A. (2013). DNMT1 mutation hot spot causes varied phenotypes of HSAN1 with dementia and hearing loss. Neurology *80*, 824–828.

Kuhn, M.W., Radtke, I., Bullinger, L., Goorha, S., Cheng, J., Edelmann, J., Gohlke, J., Su, X., Paschka, P., Pounds, S., et al. (2012). High-resolution genomic profiling of adult and pediatric core-binding factor acute myeloid leukemia reveals new recurrent genomic alterations. Blood *119*, 67–75.

Leonhardt, H., Page, A.W., Weier, H.U., and Bestor, T.H. (1992). A targeting sequence directs DNA methyltransferase to sites of DNA replication in mammalian nuclei. Cell *71*, 865–873.

Li, E., Beard, C., and Jaenisch, R. (1993). Role for DNA methylation in genomic imprinting. Nature *366*, 362–365.

Li, Y., Liu, X., Guo, X., Liu, X., and Luo, J. (2017). DNA methyltransferase 1 mediated aberrant methylation and silencing of SHP-1 gene in chronic myelogenous leukemia cells. Leuk. Res. *58*, 9–13.

Liu, B., Sun, L., Liu, Q., Gong, C., Yao, Y., Lv, X., Lin, L., Yao, H., Su, F., Li, D., et al. (2015). A cytoplasmic NF-kappaB interacting long noncoding RNA blocks IkappaB phosphorylation and suppresses breast cancer metastasis. Cancer Cell *27*, 370–381.

Lyko, F. (2018). The DNA methyltransferase family: a versatile toolkit for epigenetic regulation. Nat. Rev. Genet. *19*, 81–92.

Mastroeni, D., Chouliaras, L., Grover, A., Liang, W.S., Hauns, K., Rogers, J., and Coleman, P.D. (2013). Reduced RAN expression and disrupted transport between cytoplasm and nucleus; a key event in Alzheimer's disease pathophysiology. PLoS One *8*, e53349.

Merry, C.R., Forrest, M.E., Sabers, J.N., Beard, L., Gao, X.H., Hatzoglou, M., Jackson, M.W., Wang, Z., Markowitz, S.D., and Khalil, A.M. (2015). DNMT1-associated long non-coding RNAs regulate global gene expression and DNA methylation in colon cancer. Hum. Mol. Genet. *24*, 6240–6253.

Milutinovic, S., Brown, S.E., Zhuang, Q., and Szyf, M. (2004). DNA methyltransferase 1 knock down induces gene expression by a mechanism independent of DNA methylation and histone deacetylation. J. Biol. Chem. *279*, 27915–27927.

Mohammad, F., Mondal, T., Guseva, N., Pandey, G.K., and Kanduri, C. (2010). Kcnq1ot1 noncoding RNA mediates transcriptional gene silencing by interacting with Dnmt1. Development *137*, 2493–2499.

Morgan, A.E., Davies, T.J., and Mc Auley, M.T. (2018). The role of DNA methylation in ageing and cancer. Proc. Nutr. Soc. *77*, 412–422.

Murray, N.R., Baumgardner, G.P., Burns, D.J., and Fields, A.P. (1993). Protein kinase C isotypes in human erythroleukemia (K562) cell proliferation and differentiation. Evidence that beta II protein kinase C is required for proliferation. J. Biol. Chem. *268*, 15847–15853.

Nan, X., Ng, H.H., Johnson, C.A., Laherty, C.D., Turner, B.M., Eisenman, R.N., and Bird, A. (1998). Transcriptional repression by the methyl-CpG-binding protein MeCP2 involves a histone deacetylase complex. Nature *393*, 386–389.

O'Leary, V.B., Hain, S., Maugg, D., Smida, J., Azimzadeh, O., Tapio, S., Ovsepian, S.V., and Atkinson, M.J. (2017). Long non-coding RNA PARTICLE bridges histone and DNA methylation. Sci. Rep. *7*, 1790.

Okazaki, Y., Furuno, M., Kasukawa, T., Adachi, J., Bono, H., Kondo, S., Nikaido, I., Osato, N., Saito, R., Suzuki, H., et al. (2002). Analysis of the mouse transcriptome based on functional annotation of 60,770 full-length cDNAs. Nature *420*, 563–573.

Otani, J., Nankumo, T., Arita, K., Inamoto, S., Ariyoshi, M., and Shirakawa, M. (2009). Structural basis for recognition of H3K4 methylation status by the DNA methyltransferase 3A ATRX-DNMT3-DNMT3L domain. EMBO Rep. *10*, 1235–1241.

Pakneshan, P., Tetu, B., and Rabbani, S.A. (2004). Demethylation of urokinase promoter as a prognostic marker in patients with breast carcinoma. Clin. Cancer Res. *10*, 3035–3041.

Pandey, R.R., Mondal, T., Mohammad, F., Enroth, S., Redrup, L., Komorowski, J., Nagano, T., Mancini-Dinardo, D., and Kanduri, C. (2008). Kcnq1ot1 antisense noncoding RNA mediates lineage-specific transcriptional silencing through chromatin-level regulation. Mol. Cell *32*, 232–246.

Pastural, E., Takahashi, N., Dong, W.F., Bainbridge, M., Hull, A., Pearson, D., Huang, S., Lowsky, R., DeCoteau, J.F., and Geyer, C.R. (2007). RIZ1 repression is associated with insulin-like growth factor-1 signaling activation in chronic myeloid leukemia cell lines. Oncogene *26*, 1586–1594.

Patel, K., Dickson, J., Din, S., Macleod, K., Jodrell, D., and Ramsahoye, B. (2010). Targeting of 5-aza-2′-deoxycytidine residues by chromatin-associated DNMT1 induces proteasomal degradation of the free enzyme. Nucleic Acids Res. *38*, 4313–4324.

Pei, H., Hu, W., Guo, Z., Chen, H., Ma, J., Mao, W., Li, B., Wang, A., Wan, J., Zhang, J., et al. (2018). Long noncoding RNA CRYBG3 blocks cytokinesis by directly binding G-actin. Cancer Res. *78*, 4563–4572.

Radtke, I., Mullighan, C.G., Ishii, M., Su, X., Cheng, J., Ma, J., Ganti, R., Cai, Z., Goorha, S., Pounds, S.B., et al. (2009). Genomic analysis reveals few genetic alterations in pediatric acute myeloid leukemia. Proc. Natl. Acad. Sci. U S A *106*, 12944–12949.

Rasmussen, K.D., and Helin, K. (2016). Role of TET enzymes in DNA methylation, development, and cancer. Genes Dev. *30*, 733–750.

Rinn, J.L., Kertesz, M., Wang, J.K., Squazzo, S.L., Xu, X., Brugmann, S.A., Goodnough, L.H., Helms, J.A., Farnham, P.J., Segal, E., et al. (2007). Functional demarcation of active and silent chromatin domains in human HOX loci by noncoding RNAs. Cell *129*, 1311–1323.

Rogakou, E.P., Pilch, D.R., Orr, A.H., Ivanova, V.S., and Bonner, W.M. (1998). DNA double-stranded breaks induce histone H2AX phosphorylation on serine 139. J. Biol. Chem. *273*, 5858–5868.

Rountree, M.R., Bachman, K.E., and Baylin, S.B. (2000). DNMT1 binds HDAC2 and a new co-repressor, DMAP1, to form a complex at replication foci. Nat. Genet. *25*, 269–277.

Schmelz, K., Wagner, M., Dorken, B., and Tamm, I. (2005). 5-Aza-2′-deoxycytidine induces p21WAF expression by demethylation of p73 leading to p53-independent apoptosis in myeloid leukemia. Int. J. Cancer *114*, 683–695.

Siegfried, Z., Eden, S., Mendelsohn, M., Feng, X., Tsuberi, B.Z., and Cedar, H. (1999). DNA methylation represses transcription in vivo. Nat. Genet. *22*, 203–206.

Somasundaram, S., Forrest, M.E., Moinova, H., Cohen, A., Varadan, V., LaFramboise, T., Markowitz, S., and Khalil, A.M. (2018). The

DNMT1-associated lincRNA DACOR1 reprograms genome-wide DNA methylation in colon cancer. Clin. Epigenetics *10*, 127.

Song, J., Teplova, M., Ishibe-Murakami, S., and Patel, D.J. (2012). Structure-based mechanistic insights into DNMT1-mediated maintenance DNA methylation. Science *335*, 709–712.

Stirzaker, C., Millar, D.S., Paul, C.L., Warnecke, P.M., Harrison, J., Vincent, P.C., Frommer, M., and Clark, S.J. (1997). Extensive DNA methylation spanning the Rb promoter in retinoblastoma tumors. Cancer Res. *57*, 2229–2237.

Stresemann, C., and Lyko, F. (2008). Modes of action of the DNA methyltransferase inhibitors azacytidine and decitabine. Int. J. Cancer *123*, 8–13.

Sun, M., Nie, F., Wang, Y., Zhang, Z., Hou, J., He, D., Xie, M., Xu, L., De, W., Wang, Z., et al. (2016). LncRNA HOXA11-AS promotes proliferation and invasion of gastric cancer by scaffolding the chromatin modification factors PRC2, LSD1, and DNMT1. Cancer Res. *76*, 6299–6310.

Venolia, L., and Gartler, S.M. (1983). Comparison of transformation efficiency of human active and inactive X-chromosomal DNA. Nature *302*, 82–83.

Walsh, C.P., Chaillet, J.R., and Bestor, T.H. (1998). Transcription of IAP endogenous retroviruses is constrained by cytosine methylation. Nat. Genet. *20*, 116–117.

Wang, J., Hua, L., Guo, M., Yang, L., Liu, X., Li, Y., Shang, X., and Luo, J. (2017). Notable roles of EZH2 and DNMT1 in epigenetic dormancy of the SHP1 gene during the progression of chronic myeloid leukaemia. Oncol. Lett. *13*, 4979–4985.

Wang, L., Zhao, Y., Bao, X., Zhu, X., Kwok, Y.K., Sun, K., Chen, X., Huang, Y., Jauch, R., Esteban, M.A., et al. (2015). LncRNA Dum interacts with Dnmts to regulate Dppa2 expression during myogenic differentiation and muscle regeneration. Cell Res *25*, 335–350.

Wang, X.X., Guo, G.C., Qian, X.K., Dou, D.W., Zhang, Z., Xu, X.D., Duan, X., and Pei, X.H. (2018). miR-506 attenuates methylation of lncRNA MEG3 to inhibit migration and invasion of breast cancer cell lines via targeting SP1 and SP3. Cancer Cell Int. *18*, 171.

Watt, F., and Molloy, P.L. (1988). Cytosine methylation prevents binding to DNA of a HeLa cell transcription factor required for optimal expression of the adenovirus major late promoter. Genes Dev. *2*, 1136–1143.

Wen, L.Z., Ding, K., Wang, Z.R., Ding, C.H., Lei, S.J., Liu, J.P., Yin, C., Hu, P.F., Ding, J., Chen, W.S., et al. (2018). SHP-1 acts as a tumor suppressor in hepatocarcinogenesis and HCC progression. Cancer Res. *78*, 4680–4691.

Werner, M.S., and Ruthenburg, A.J. (2015). Nuclear fractionation reveals thousands of chromatin-tethered noncoding RNAs adjacent to active genes. Cell Rep. *12*, 1089–1098.

Wilson, C., and Kanhere, A. (2021). 8q24.21 locus: a paradigm to link non-coding RNAs, genome polymorphisms and cancer. Int. J. Mol. Sci. *22* (3), 1094, https://doi.org/10.3390/ijms22031094.

Xu, M., Xu, X., Pan, B., Chen, X., Lin, K., Zeng, K., Liu, X., Xu, T., Sun, L., Qin, J., et al. (2019). LncRNA SATB2-AS1 inhibits tumor metastasis and affects the tumor immune cell microenvironment in colorectal cancer by regulating SATB2. Mol. Cancer *18*, 135.

Yang, M.Y., Liu, T.C., Chang, J.G., Lin, P.M., and Lin, S.F. (2003). JunB gene expression is inactivated by methylation in chronic myeloid leukemia. Blood *101*, 3205–3211.

Yin, W., Rossin, A., Clifford, J.L., and Gronemeyer, H. (2006). Co-resistance to retinoic acid and TRAIL by insertion mutagenesis into RAM. Oncogene *25*, 3735–3744.

Yu, J., Peng, Y., Wu, L.C., Xie, Z., Deng, Y., Hughes, T., He, S., Mo, X., Chiu, M., Wang, Q.E., et al. (2013). Curcumin down-regulates DNA methyltransferase 1 and plays an anti-leukemic role in acute myeloid leukemia. PLoS One *8*, e55934.

Yu, W., Gius, D., Onyango, P., Muldoon-Jacobs, K., Karp, J., Feinberg, A.P., and Cui, H. (2008). Epigenetic silencing of tumour suppressor gene p15 by its antisense RNA. Nature *451*, 202–206.

iScience, Volume *24*

Supplemental information

A long intergenic non-coding RNA regulates nuclear localization of DNA methyl transferase-1

Rhian Jones, Susanne Wijesinghe, Claire Wilson, John Halsall, Triantafillos Liloglou, and Aditi Kanhere

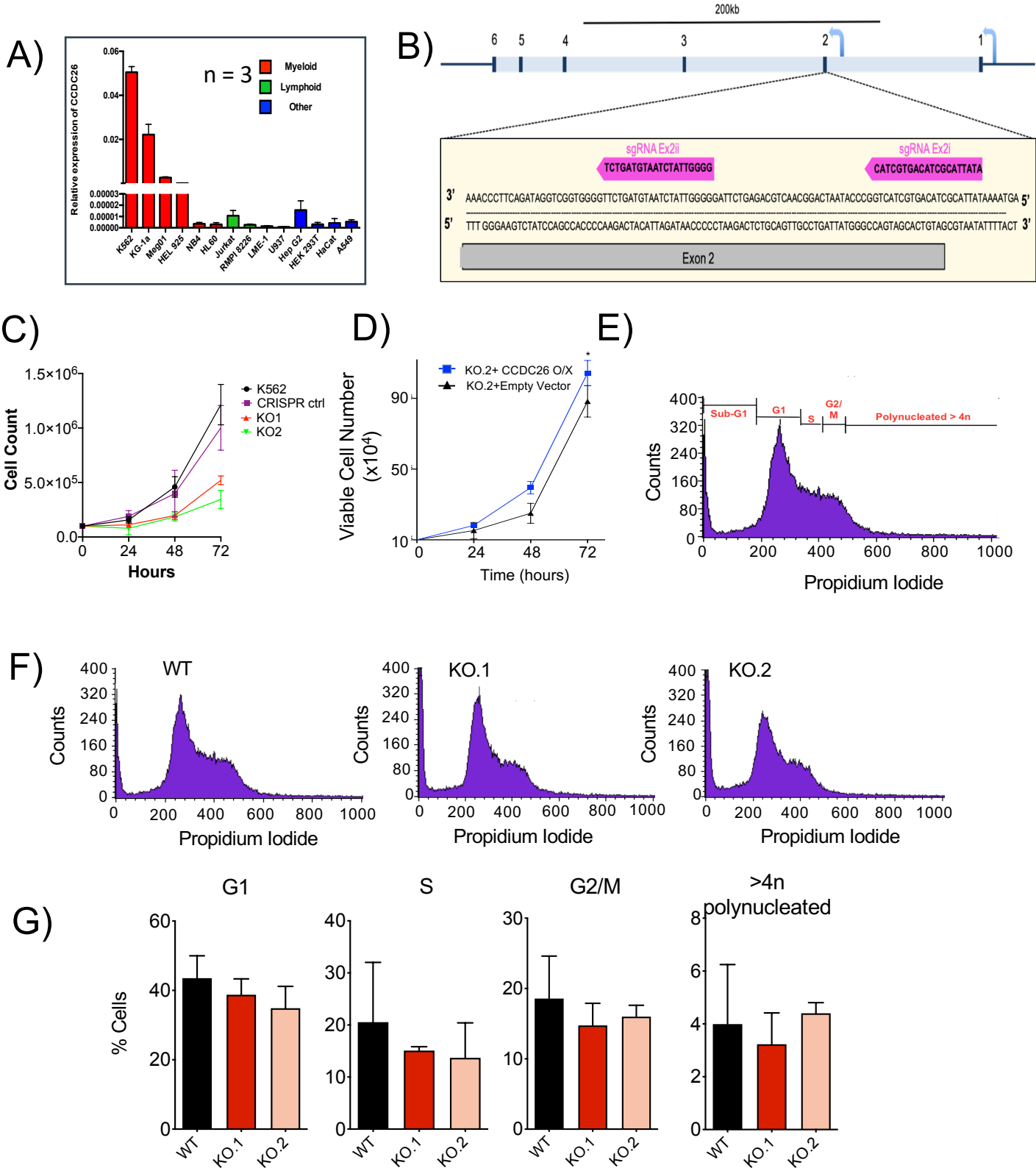

Figure S1.The effect of CCDC26 knockout on cell growth and cell cycle, Related to Figure 1

(A) *CCDC26* expression in 14 different cell-lines of diverse origins. Expression was measured using qRT-PCR assays and normalised against expression levels of Actin.

(B) Schematic of the *CCDC26* gene showing that TSS2 was targeted with two sgRNAs simultaneously using CRISPR/Cas9 technology to establish *CCDC26* KO cell lines.

(C) Growth curves for K562, CRISPR control and CCDC26 knockouts.

(D) Growth curves of KO.2 expressing CCDC26 from an exogenous vector (CCDC26 o/x) and empty vector.

(E) A schematic showing how the number of cells in different cell cycle stages are calculated after FACS analysis.

(F) Histograms showing distribution of WT and KO cells in different cell cycle stages after propidium iodide staining and FACS analysis.

(G) Plots showing the percentage of WT, KO.1 and KO.2 cells in each stage of the cell cycle following propidium iodide staining and FACS analysis. Values represent the mean ± standard deviation (n=3) (unpaired, two-tailed *t* test).

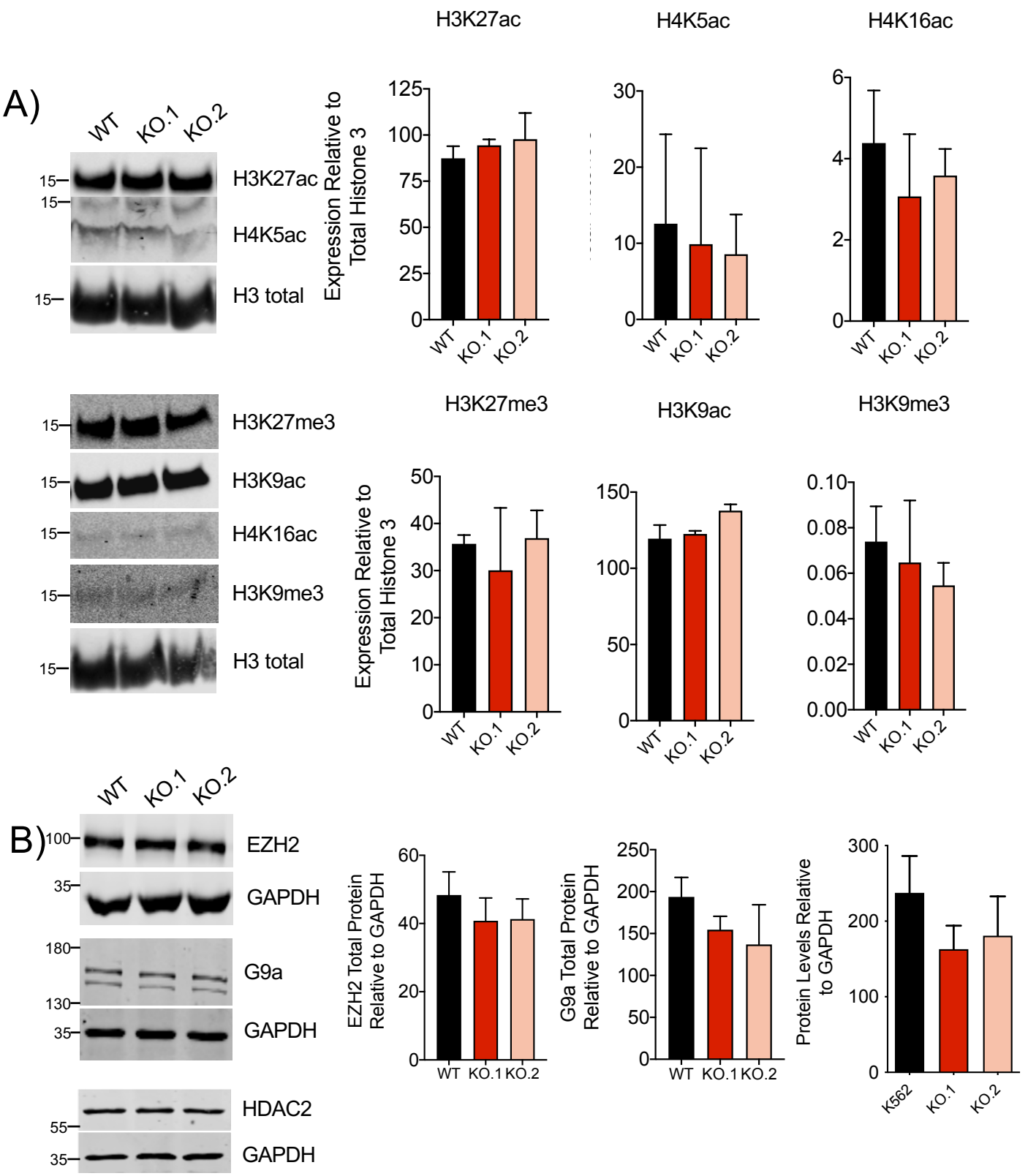

Figure S2. CCDC26 knockout has no effect on genomic level of histone modifications, Related to Figure 2

(A) Immunoblotting on histone protein isolated from WT and CCDC26 KO cells using antibodies against common histone modifications (anti-H3K27ac, -H4K5ac, -H3K27me3, -H3K9ac, -H4K16ac and H3K9me3). Levels were measured relative to total histone H3 levels. Values represent the mean ± standard deviation (n=3) (unpaired, two-tailed *t* test).

(B) Total protein levels of histone modifying enzymes, EZH2, G9a and HDAC2 measured relative to GAPDH by immunoblotting, are unchanged in WT and *CCDC26* KO cells. Values represent the mean ± standard deviation (n=3) (unpaired, two-tailed *t* test).

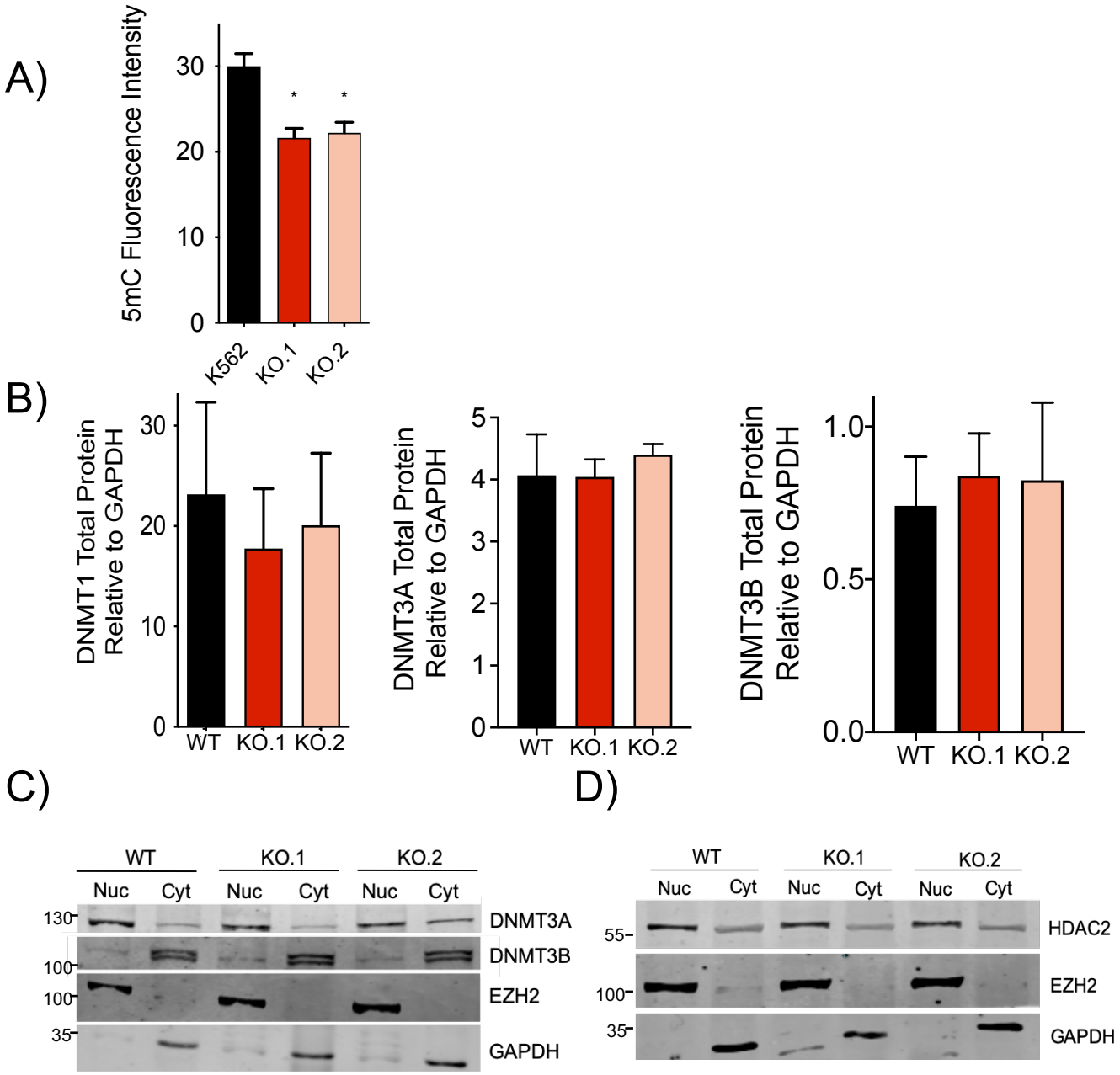

Figure S3. CCDC26 removal leads to DNA hypomethylation but has no effect on DNMT levels, Related to Figure 2

(A) 5mC Immunofluorescence intensity measurements in *CCDC26* KO cells compared to WT. 5mC fluorescence intensity was measured in 2D confocal images for 200 individual nuclei, per replicate, using FIJI image analysis software. Values represent the mean ± standard deviation (n=3). * P<0.05 (unpaired, two-tailed *t* test).

(B) Plots showing total protein levels of DNMT1, DNMT3a and DNMT3b relative to GAPDH in WT K562, KO.1 and KO.2 cells by immunoblotting. Values represent the mean ± standard deviation. * P<0.05 (unpaired, two- tailed *t* test) (n=3).

(C) Immunoblotting for DNMT3A and DNMT3B on nuclear and cytosolic protein fractions show no significant difference in subcellular localization between WT and *CCDC26* KO cells. EZH2 and GAPDH are used as nuclear and cytosolic markers respectively (nuc = nuclear protein fraction; cyt = cytosolic protein fraction).

(D) Immunoblotting for HDAC2 on nuclear and cytosolic protein fractions show no significant difference in subcellular localization between WT and *CCDC26* KO cells. EZH2 and GAPDH are used as nuclear and cytosolic markers respectively (nuc = nuclear protein fraction; cyt = cytosolic protein fraction).

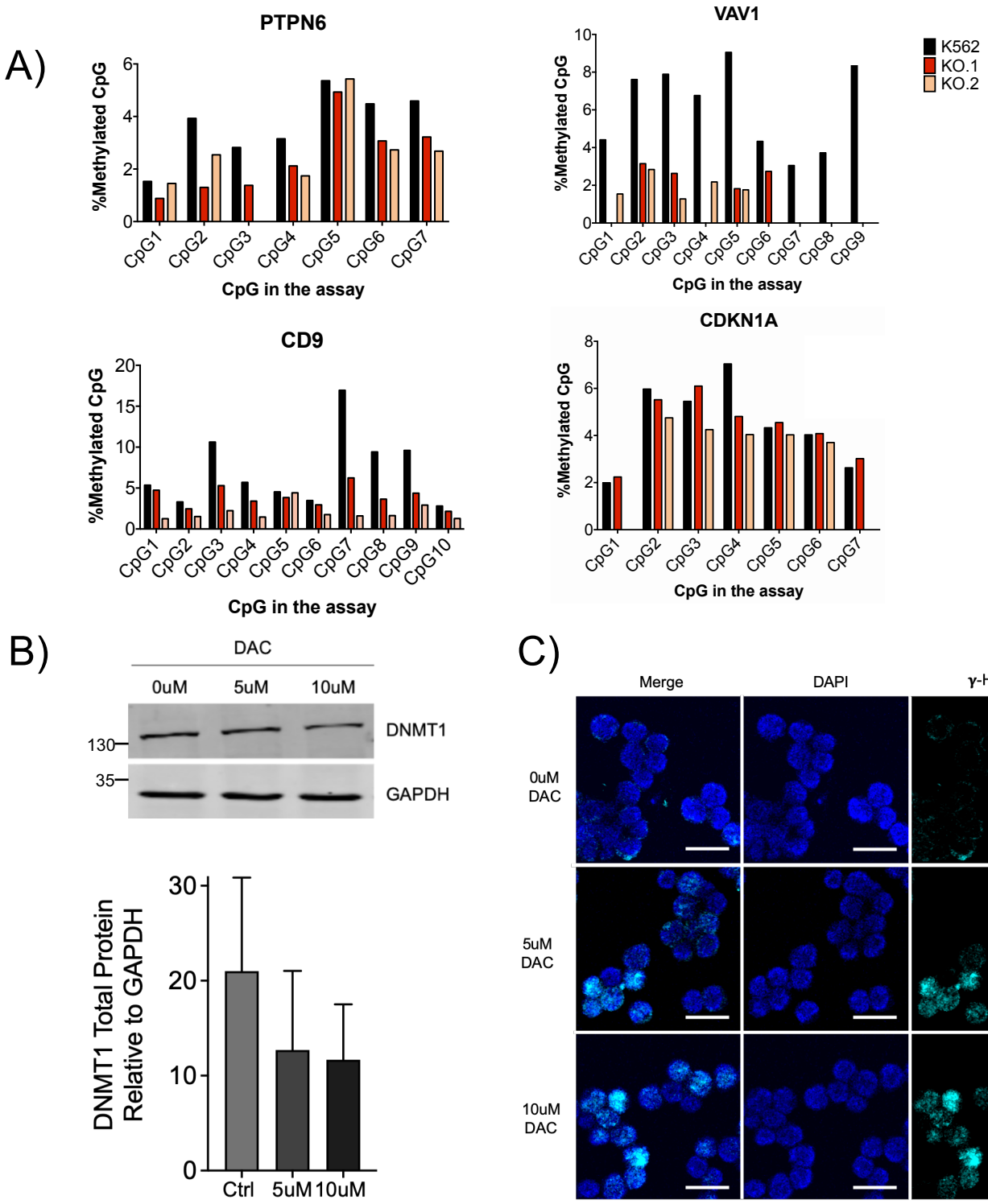

Figure S4. DNMT1 inhibition by DAC has the same effect as CCDC26 knockout, Related to Figure 3

(A) DNA methylation profiling at individual gene promoters using bisulphite conversion and pyrosequencing. Percentage of methylated CpGs in individual promoters in K562 and the two knockouts is plotted as a bar chart.

(B) Immunoblotting for DNMT1 total protein levels in cells treated with 0uM 5uM and 10uM DAC, measured relative to GAPDH. DNMT1 levels are slightly reduced in cells treated with 5uM and 10uM DAC. Values represent the mean ± standard deviation (n=3) (unpaired, two-tailed *t* test).

(C) Confocal images demonstrating the results of anti-γ-H2AX immunofluorescence. Cells treated with 0uM, 5uM and 10uM DNMT1 inhibitor, DAC, were stained with DAPI nuclear stain (blue) and anti-γ-H2AX antibody (cyan). Increased numbers of γ-H2AX foci are present in the cells treated with 5uM and 10uM DAC Scale bar = 25um.

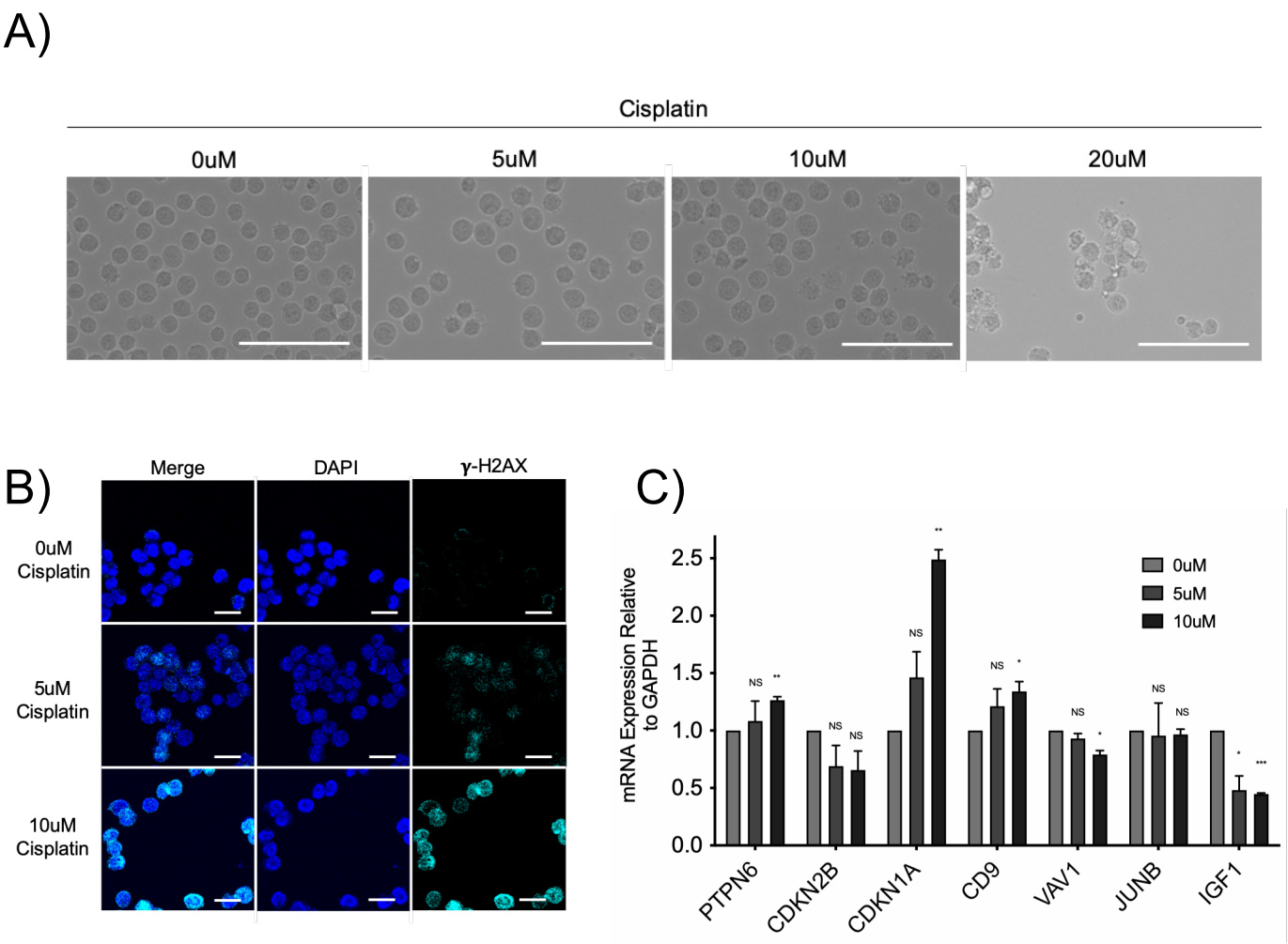

Figure S5. Cisplatin induced DNA damage has no effect on DNMT1 regulated genes, Related to Figure 4

A) Brightfield microscopy images of K562 cells treated with increasing concentrations of DNA damage-inducing drug, cisplatin. Cells appear increasingly distressed with increasing cisplatin concentrations. Scale bar = 100um.

B) Confocal images demonstrating the results of anti-γ-H2AX immunofluorescence. Cells treated with 0uM, 5uM and 10uM DNA damage-inducing drug, cisplatin, were stained with DAPI nuclear stain (blue) and anti-γ-H2AX antibody (cyan). Increased numbers of γ-H2AX foci are present in the cells treated with 5uM and 10uM cisplatin. Scale bar = 25um.

C)A plot showing expression levels of various genes whose expression have previously been shown to be impacted by DNMT1 depletion or DNA hypomethylation in myeloid leukemia. Levels are measured relative to GAPDH in cells treated with 0uM, 5uM and 10uM cisplatin. Values represent the mean ± standard deviation. * P<0.05; **P<0.01; ***P<0.001; NS = Not significant (unpaired, two- tailed *t* test).

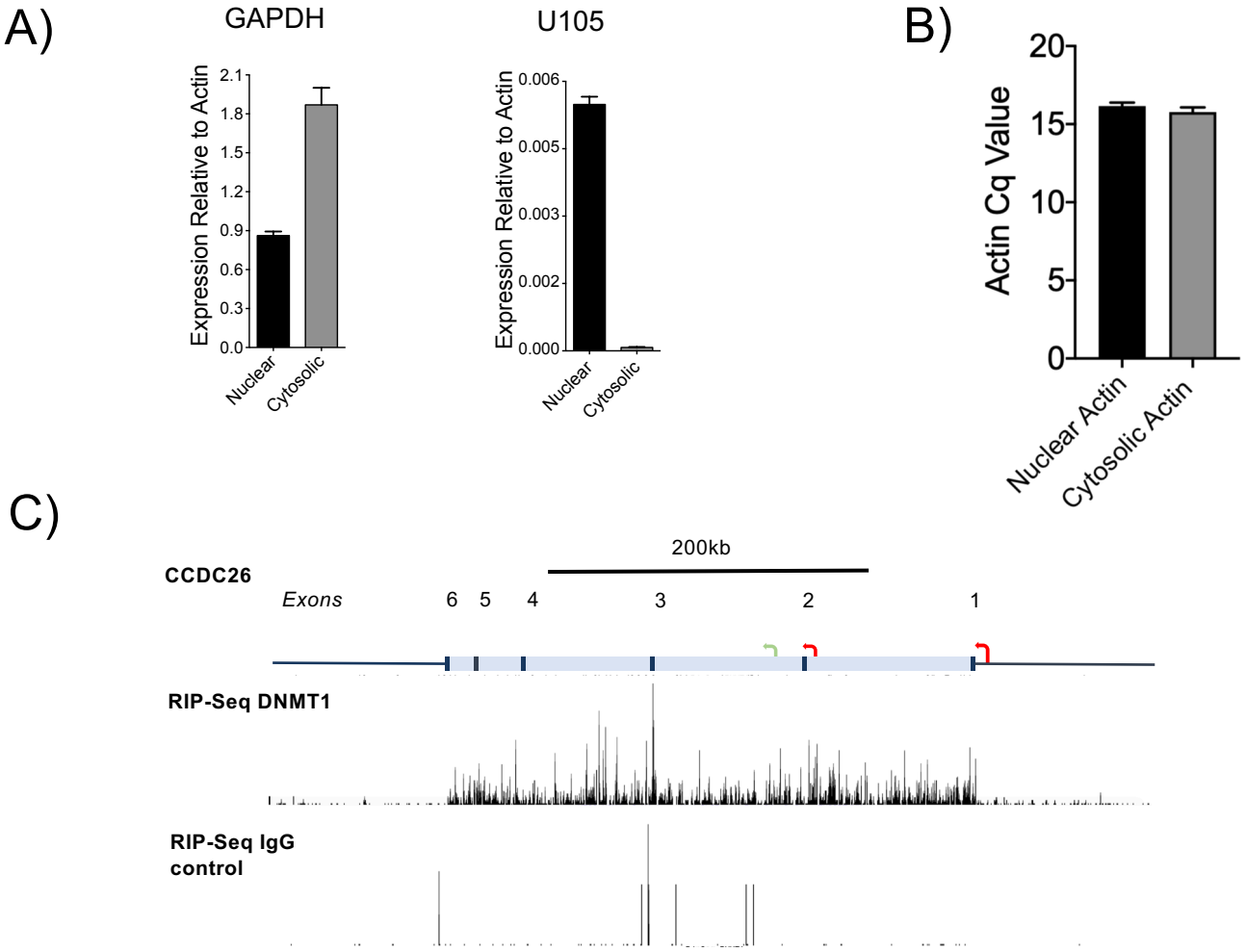

Figure S6. DNMT1 interacts with lincRNA CCDC26, Related to Figure 5

(A) Plots showing RNA levels of GAPDH and U105 in cytosolic and nuclear fractions relative to Actin level. Values represent the mean ± standard deviation. * $P<0.05$ (unpaired, two- tailed *t* test, n=3).

(B) Cq measurements for K562 nuclear and cytosolic RNA fractions generated by qRT-PCR using Actin primers.

(C) Re-analysis of a previously published DNMT1 RIP-seq data set, performed in HL60 cells. Re-mapping the cellular RNAs pulled down with either a DNMT1 antibody or an IgG control antibody shows enrichment for *CCDC26* in DNMT1-RNA, compared to IgG control. (Di Ruscio et al. 2013) (GEO Accession: GSE32162). Data available at NCBI Gene Expression Omnibus (GEO).

(D) Re-analysis of a previously published DNMT1 fRIP-seq data set, performed in K562 cells shows high enrichment of *CCDC26* in DNMT1-bound RNAs (Hendrickson et al. 2016) (GEO Accession: GSE67963). Data available at NCBI Gene Expression Omnibus (GEO).

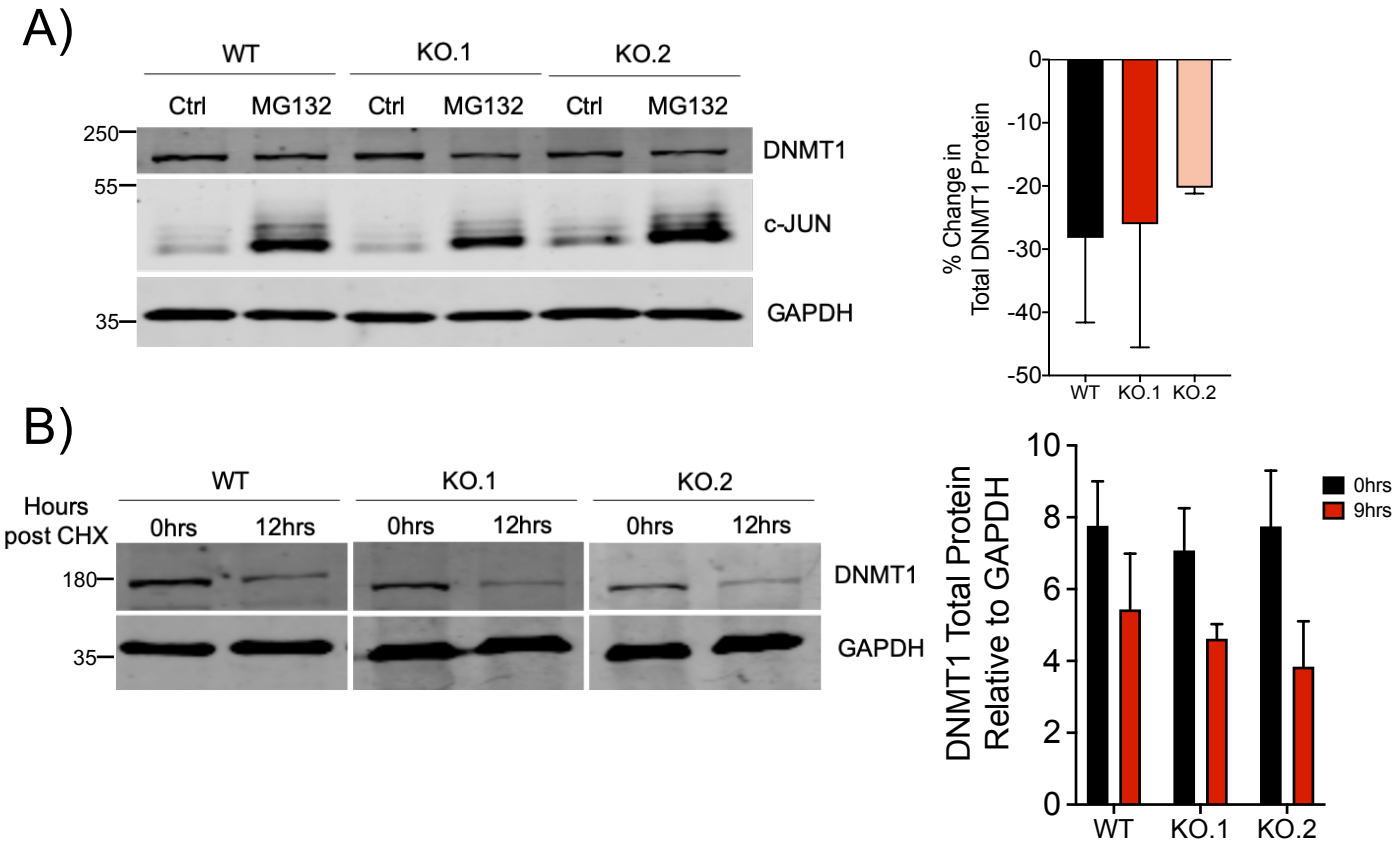

Figure S7. DNMT1 stability is not affected by CCDC26 knockout, Related to discussion in main text.

(A) Immunoblotting for DNMT1 total protein levels in WT and CCDC26 KO cells following treatment with 10uM of proteosomal inhibitor MG132. DNMT1 protein levels fell in both WT and KO cells. The difference in the extent to which DNMT1 levels fall was not statistically significant between cell lines. Immunoblotting for c-JUN was also performed as a control to show that the MG132 inhibitor was working. C-JUN levels rose upon MG132 treatment in both WT and KO cells. Protein levels were measured relative to the housekeeping protein, GAPDH. Values represent the mean ± standard deviation (unpaired, two-tailed *t* test, n=3).

(B) Immunoblotting for DNMT1 total protein levels on WT and CCDC26 KO cells treated with cycloheximide (CHX) for 0hrs and 12hrs. The difference in the extent to which DNMT1 levels fall was not statistically significant between WT and KO cells. Values represent the mean ± standard deviation (unpaired, two-tailed *t* test, n=3).

Table S1. Primers, related to figure 1, figure 3 and figure 5

All primers were purchased from Sigma and are shown 5'-3'

Primer	Forward	Reverse
CCDC26_RNAFISH	CCTGCCACACTGGGAAAGAT	GAAATTAATACGACTCACTATAGTTGACTTCCCA GGAGCGAA
CCDC26_All (all isoforms)	ATGGAAAGATTGTGCCTGCAG	CTCGATCTTTCCCAGTGTGG
CCDC26_Set1-2 (isoforms 1 and 2)	TCAGGCAACTGCAGAGTCTTAG	ACCCAGGCTTGTCTCATCTC
CCDC26_Set3 (isoform 3)	AGATCAGCTATGAAGGCCTGAG	CTCGATCTTTCCCAGTGTGG
CCDC26_Set4 (isoform 4)	TTCAAGAATGGCCTTTTAAAGGACC	CTCGATCTTTCCCAGTGTGG
GAPDH	GGAGCGAGATCCCTCCAAAAT	GGCTGTTGTCATACTTCTCATGG
U105	CCCTATCTCTCATGATGAAC	CCCATCTCTTCTTCAGAGCG
DNMT1	GCGGTATACCCACCATGACA	AGGCTTTGCCGGCTTCC
DNMT3A	GTTGTGAGAAGGAATGGGCG	TTGGCTTTCTTCTCAGCCGTAT
DNMT3B	CACTCTGTCCTGGGTGCTG	GTCTCCCTTCATGCTTTCCAAG
PTPN6	AACAGCCGTGTCATCGTCAT	ATCAGGTCTCCATTGTCCAGC
CDKN2B	TGGGGGCGGCAGCGATGAG	AGGTGGGTGGGGGTGGGAAAT
CDKN1A	AGCATGACAGATTTCTACCACTC	GATGTAGAGCGGGCCTTTGA
CD9	CATCTGTATCCAGCGCCAGG	CCGGCAAGCCAGAAGATGAA
VAV1	CTTACGGAGCTGGTGGAGTT	ACTTTGTGCTTCCCACTGCT
JUNB	CTGCTGGAAACAGACTCGATTC	CCACAGTACGGTGCAGAGAG
IGF1	TGCTCTCAACATCTCCCATCTC	TGGTGTGCATCTTCACCTTCA
Actin B	TACTCCTGCTTGCTGATCCA	GATCATTGCTCCTCCTGAGC

Table S2. Primary Antibodies, related to figure 1, 2, 3, 4 and 5

WB = western blot; IF = immunofluorescence; IP = immunoprecipitation; RIP = RNA immunoprecipitation; M = monoclonal; P = polyclonal

Antibody	Use	Working Dilution	Origin	Company	Catalog No.	Clonality
GAPDH	WB	1:1000	Mouse	ThermoFisher Scientific	MA5-15738	M
DNMT1	WB	1:1000	Mouse	NovusBio	NB100-56519	M
DNMT3A	WB	1:1000	Rabbit	NovusBio	NB100-265SS	P
DNMT3B	WB	1:1000	Rabbit	BioVision	3275	P
EZH2	WB	1:1000	Rabbit	Cell Signaling	#5246	M
HDAC2	WB	1:700	Rabbit	Santa Cruz	sc-7899	P
Caspase 9	WB	1:1000	Rabbit	Cell Signaling	#9508	M
H3K27ac	WB	1:1000	Rabbit	Abcam	ab4729	P
H4K5ac	WB	Generated and kindly gifted by Dr John Halsall (Turner Group)				
H3K27me3	WB	1:1000	Mouse	Abcam	ab6002	M
H3K9ac	WB	Generated and kindly gifted by Dr John Halsall (Turner Group)				
H4K16ac	WB	1:1000	Rabbit	Abcam	ab109463	M
H3K9me3	WB	1:500	Rabbit	Millipore	07-442	P
Histone H3	WB	1:5000	Rabbit	Abcam	ab1791	P
c-JUN	WB	1:1000	Rabbit	Cell Signaling	#9165	M
DNMT1	IF	1:10	Mouse	NovusBio	NB100-56519	M
5mC	IF	1:250	Mouse	Epigentek	A-1014	M
γ-H2AX	IF	1:100	Mouse	Millipore	05-636-AF555	M
DNMT1	RIP	/	Mouse	NovusBio	NB100-56519	M
IgG	RIP	/	Mouse	Sigma	18765-5MG	/

Table S3. Secondary Antibodies, figure 1, 2, 3, 4 and 5
WB = Western Blot; IF = Immunofluorescence

Antibody	Use	Working Dilution	Company	Catalog No.
Anti-rabbit IgG (H+L) (DyLight™ 800 4X PEG Conjugate)	WB	1:10,000	Cell Signaling	5151
Anti-mouse IgG (H+L) (DyLight™ 680 Conjugate)	WB	1:10,000	Cell Signalling	5470
Alexa Fluor 488 donkey anti-rabbit IgG (H+L)	IF	1:500	Invitrogen	A21206
Alexa Fluor 633 goat anti-mouse IgG (H+L)	IF	1:500	Invitrogen	1010093

Table S4: Sequences of primers for Pyrosequencing Methylation Analysis, related to figure 3

Primer name	Sequence 5'-> 3'	Modification
VAV1meth-F	GGTAAAGAAGAGGAAGTGGTA	
VAV1meth-Rb	AACTCCACAACTCCATAACTAC	5' biotin
VAV1meth-S	AGAAGAGGAAGTGGTAGTATT	
IGF2meth-Fb	GAAGGATATAATTTTGTTGAGAA	5-biotin
IGF2meth-R	TCCCTTTAAATAAATCTAACTACTA	
IGF2meth-S	AACTACTACTATCAATACACC	
CD9meth-F	GGGGAAGAGTTTTTTAAAGTAG	
CD9meth-Rb	CACTCCCTACCACTTTTACC	5' biotin
CD9meth-S	AAGAGTTTTTTAAAGTAGAA	
CDKN1Ameth-Fb	TTAGTGGGGAAATGTGTTTA	5' biotin
CDKN1Ameth-R	CAAACCCAAACTCCTAACTAC	
CDKN1Ameth-S	CCCAAACTCCTAACTACC	
PTPN6meth1-F	AGTTTTTAGGAAAAGGATAGG	
PTPN6meth1-Rb	TCCAAATAACTCCTCCTCTC	5' biotin*
PTPN6meth1-S	TTTAGGAAAAGGATAGGTG	

F: forward PCR primer, R: Reverse PCR primer, S: pyrosequencing primer, b: biotinylated

Table S5. Pyrosequencing Methylation Analysis, related to figure 3

Promoter	Cell line	Mean Rank	p-value
CD9	K562	3	<0.001
	KO.1	1.9	
	KO.2	1.1	
CDKN1A	K562	2.29	0.004
	KO.1	2.71	
	KO.2	1	
PTPN6_1	K562	2.86	0.021
	KO.1	1.57	
	KO.2	1.57	
VAV1	K562	3	0.001
	KO.1	1.61	
	KO.2	1.39	

Transparent Methods

Cell Culture

K562 cells were maintained in RPMI 1640 media (GIBCO, ThermoFisher Scientific), supplemented with 10% Fetal Bovine Serum (FBS) and 1% penicillin-streptomycin (10,000 U/ml), at 37°C, 5% CO_2. Cells were monitored daily, passaged (split) every ~48 hours and seeded at 2.5 x 10^5 cells in growth media. A hemocytometer was used to observe and count cells for seeding. All cell centrifugations were performed at 1200rpm, for 5 minutes at room temperature unless stated otherwise.

To monitor cell growth, 10^5 cells/ml were seeded into a 6 well-plate and viable cells were counted after 24, 48 and 72 hours. Trypan Blue dye exclusion was used to distinguish viable cells. Before counting, 10ul cell suspension was mixed with 10ul 0.4% Trypan Blue solution (ThermoFisher, Cat: 15250061). 10ul of this mix was then applied to a hemocytometer and cells were counted, excluding those that appeared blue.

Cells were seeded at a density of 2.5 x 10^5 cells/ml and grown in the presence of various inhibitors and drugs. All inhibitors were prepared in a sterile tissue culture hood, and all solvents were filter sterilized before preparing stocks. Control cells were grown in the presence of the equivalent volume of solvent in which each inhibitor was dissolved (E.g. DMSO or H_2O). Upon harvesting after treatment, cells were washed in PBS three times, centrifuging between washes. Cells were grown in growth media containing a final concentration of either 0uM (control), 5uM or 10uM cisplatin (Millipore, Cat: 232120) for 24 hours, before harvesting. A 10mM cisplatin stock was freshly prepared in H_2O for each use. Cells were grown in growth media containing a final concentration of either 0uM (control), 5uM or 10uM 5-Aza-2'-deoxycytidine (DAC) for 48 hours, before harvesting. A 220mM DAC stock was freshly prepared in DMSO for each use.

All cell transfections were similarly performed via electroporation using the Cell Line Nucleofector Kit V (Lonza, Cat: VVCA-1003). For each transfection, 10^6 cells were centrifuged and washed once in 500ul PBS. Stable CCDC26 overexpression (O/x) cell lines were

prepared by first ligating a spliced CCDC26 transcript (isoform 1) into a modified pEF6 plasmid (ThermoFisher #V96220, myc epitope and His-tag were removed previously). Briefly, the resulting plasmid, as well as an empty control pEF6 plasmid lacking CCDC26, were used to transfect both WT and CCDC26 KO cells via electroporation, which were subsequently selected with Blasticidin S HCl (TOKU-E B001). For use in this project, these cell lines were grown in growth media supplemented with a final concentration of 4ug/ml Blasticidin S HCl. For this purpose, a 25mg/ml Blasticidin S HCl stock was prepared in H_2O in sterile conditions and stored at -20°C. CCDC26 overexpression was confirmed via qRT-PCR.

For CRISPR/CAS9 mediated knockouts sgRNA targeting CCDC26 was designed using Wellcome Trust Sanger Institute Genome Editing database (WGE) (Hodgkins *et al*, 2015). sgRNA was selected with minimum off-target effects and close to transcription start site of isoform-1. K562 cells were electroporated with 5µg pX459 vector (Addgene) containing sgRNA targeting CCDC26. Transfected cells were selected for 3 days in a medium containing 0.5 µg/ml puromycin. Selected cells were serially diluted to single cells and were let to grow till colonies were grown. Homozygous mutations were confirmed by amplifying targeted loci using RT–PCR. RT–PCR products were cloned into pJET1.2 blunt vector (ThermoFisher Scientific), and at least 10 bacterial colonies were picked up for genotyping. For CRISPR controls, K562 cells were transfected with pX459 vector without any sgRNAs and cell lines were created similarly as in case of knockouts.

Propidium iodide Fluorescence Activated Cell Sorting (FACS) cell cycle analysis

For cell cycle analysis, ~300,000 cells were centrifuged in FACS tubes. 300ul cold, cell cycle buffer (30µg propidium iodide (PI), 1% (w/v) sodium citrate, 0.1mM $NaCl_2$, 0.1% Triton X-100) was added to the pellet, and gently vortexed, before storing at 4°C for ~24 hours in the dark, to allow PI staining. Depending on the cell cycle stage, cells contain different amounts of DNA. Cells display PI fluorescence that is proportional DNA content and therefore PI fluorescence can be used as a proxy to DNA content. DNA content measurements was performed using a

BD FACS Calibur flow cytometer and data analysis conducted using the BD Cell Quest software (BD Biosciences). For every analysis, 50000 cells were counted with gating to only include single cells. For each sample, extent of propidium iodide staining or DNA content was plotted as a histogram. The cell cycle stages were defined based on DNA content as follows: sub-G1: DNA content < 2n; G1:DNA content = 2n; G2/M:DNA content=4n; Multinucleated cells > 4n. The remaining percentage was attributed to S-phase. The cell cycle boundaries were manually optimized on WT K562 DNA histogram and uniformly applied to all samples as shown in the Figure S1C. The percentage of cells in each cell cycle stage was automatically calculated based on area under curve by BD Cell Quest software. The final values were calculated as mean of three independent experiments.

Cell Fixation

4 x 10^6 cells were harvested and centrifuged at 1200rpm for 5 minutes at room temperature. Growth media was removed from the pellet, which was then washed in 1ml PBS and centrifuged again as before. The PBS was removed, and the pellet was re-suspended in 50ul PBS. 1ml of a 3:1 mix of Methanol:Acetic Acid fixative was added, gently mixed and incubated at room temperature for 10 minutes exactly. This was followed immediately with centrifugation, followed by three washes with 1ml PBS. Fixed cells were stored in 3ml 70% Ethanol at 4°C at least overnight before use and stored at 4°C for no longer than 3 months.

Immunofluorescence

Approximately 2.5x10^5 fixed cells per slide were aliquoted into sterile microcentrifuge tubes, which were centrifuged for 5 minutes at 7000 rpm, room temperature. The supernatant was removed and the pellet was re-suspended in 200ul PBS. Samples were then spun down onto microscope slides via cyto-centrifugation for 7 minutes at 350rpm.

Cells were blocked by pipetting 50ul of 5% Bovine serum albumin (BSA) (Promega, Cat: W3841) directly onto slides, and incubating for 1 hour at room temperature, followed by a brief

wash in PBS. 50ul of primary antibody (Table S2) diluted in 5% BSA was then pipetted onto each slide and temporarily covered with a 22mm x 22mm coverslip. Slides were placed into a moist chamber and incubated overnight at 4°C. For 5mC immunofluorescence, slides were heated at 94°C for 3 minutes prior to loading primary antibody, in order to separate DNA strands to allow binding.

The following morning, coverslips were removed and slides were carefully washed three times in PBS. Approximately 80ul of the appropriate secondary antibody, diluted in PBS (Table S3) was then pipetted onto slides, sealed temporarily with a coverslip and incubated at room temperature for 1 hour in the dark. This was followed by three PBS washes and a final single wash in H_2O. After allowing slides to dry, 10ul of SlowFade® Gold anti-fade reagent (Invitrogen RNA FISH Kit, Cat. No. F32956) and 1ug/ml DAPI were added to the slide which was then covered with a coverslip and sealed with nail polish.

RNA Fluorescence in situ Hybridization (FISH)

A fluorescently labelled *CCDC26* RNA probe was generated using the FISH Tag RNA Multicolor Kit, Alexa Fluor dye combination (Invitrogen, Cat. No. F32956), following the manufacturers guidelines. A *CCDC26* exon 6 DNA template was generated by performing a PCR using Red Mix (Bioline, Cat. No. BIO25043) WT K562 cDNA and *CCDC26*-specific primers that incorporated a T7 RNA polymerase promoter at the 5'-end of the DNA strand to be later transcribed (Table S1). PCR products ran on a 1% agarose gel and gel purified using the QIAquick Gel Extraction Kit (Cat. No. 28704), following the manufacturers guidelines. The subsequent *CCDC26* DNA template was subsequently used in the first in vitro transcription step of probe generation as directed by the FISH Tag RNA Multicolor Kit.

200ul fixed cells per slide were aliquoted into sterile microcentrifuge tubes, which were centrifuged for 5 minutes at 7000 rpm, room temperature. The supernatant was removed, and the pellet was re-suspended in 500ul Wash Buffer A (5ml 20X nuclease free saline-sodium

citrate (SSC), 5ml deionized formamide, 40ml nuclease-free H_2O). Cells were centrifuged as before and the pellet resuspended in 100ul Hybridization Buffer (1g dextran sulphate, 1ml deionized formamide, 1ml 20X nuclease-free SSC, 8ml nuclease-free H_2O) containing 1ug/ml of probe. This was mixed well by pipetting and incubated overnight, in the dark at 37°C. The following morning, the cells were centrifuged and washed with 500ul Wash Buffer A. Following another centrifugation, the pellet was resuspended in 500ul Wash Buffer A and incubated in the dark, at 37°C for 30 minutes. The cells were centrifuged, and the buffer removed. Cells were then resuspended in 200ul PBS and spun down onto microscope slides via cyto-centrifugation for 7 minutes at 350rpm. 10ul of SlowFade® Gold anti-fade reagent (Invitrogen RNA FISH Kit, Cat. No. F32956) and 1ug/ml DAPI were added to the slide which was then covered with a coverslip and sealed with nail polish.

Confocal Microscopy

Slides were imaged using a Leica TCS SP8 Confocal microscope, using either 20X, 40X or 63X objectives. The brightfield microscope setting was used to visualise cell membrane boundaries. FIJI image analysis software was used to visualise and analyse confocal images.

RNA Extraction

An RNase-free environment was maintained for all RNA work by treatment of equipment and work surfaces with RNase *Zap*, RNase decontamination solution (ThermoFisher Scientific, Cat. No. AM9780).

All RNA was extracted using the QIAGEN RNeasy Mini Kit (Cat: 74106), following manufacturers guidelines. RNA was eluted in 30ul RNase-free H_2O and concentrations were determined using a NanoDrop ND-100 spectrophotometer (Thermo Scientific). RNA quality was determined by running ~200-300ng on a 1% agarose gel.

Nuclear and Cytosolic RNA Extraction

For extraction of nuclear and cytosolic RNA fractions, approximately 10^7 cells were harvested by centrifuging at 1200rpm at room temperature for 5 minutes, washing in 1ml PBS and centrifuging again. As much supernatant as possible was removed from the cell pellet, which was then re-suspended in 1ml of cold (4°C) Buffer RLN (50mM Tris-HCl (pH.8), 1.5mM $MgCl_2$, 140mM NaCl, 0.5% NP-40, 100U/ml RNase inhibitor) and incubated on ice for 5 minutes. 250ul of the mix was then pipetted into four eppendorfs labelled “nuclear”. These were centrifuged for 2 minutes at 3700rpm, 4°C. Approximately 500ul of supernatant collected from all four eppendorfs was collected as cytosolic fraction, taking extra care not to disturb the nuclear pellets. Each of the four nuclear pellets were washed twice with 100ul Buffer RLN, centrifuging for 2 minutes at 3200rpm, 4°C between washes. 200ul and 600ul Buffer RLT (containing 1% β-mercaptoethanol, QIAGEN RNeasy Mini Kit) was added to nuclear and cytosolic fractions respectively and vortexed vigorously. The nuclear pellets were further homogenized using a 1ml syringe and needle (21G x 1.5” – Nr.2., 0.8mm x 40mm). The fractions were then centrifuged for 3 minutes at maximum speed to remove cell debris, and the supernatants were removed and mixed with 1X volume 70% ethanol. The extraction was continued using the QIAGEN RNeasy Mini Kit, following manufacturers guidelines.

All freshly extracted RNA was treated with DNase I using the Sigma, amplification grade DNase I kit (Cat: AMPD1), following the kit guidelines, and converted into cDNA using the Bioline-Tetro cDNA Synthesis Kit (Cat. No. BIO-65042) following the manufacturers guidelines.

Quantitative Real-Time Polymerase Chain Reaction (qRT-PCR)

qRT-PCRs were performed in 96-well plates. 20ng of cDNA made up to 6.8ul with dH_2O was added to each well (in triplicate) with 1.6ul forward primer (5uM), 1.6ul reverse primer (5uM) and 10ul SensiFAST SYBR Hi-ROX mix (Bioline, Cat: BIO92020). The plate was then loaded into an Agilent AriaMax real time PCR machine (Agilent Technologies) and the qRT- PCR was

performed (1 cycle at 95.0°C for 2 minutes, followed by 40 cycles at 95.0°C for 5 seconds, 60.0°C for 10 seconds and 72.0°C for 10 seconds).

The average cycle threshold (Ct) values from each technical triplicate were calculated and used to determine expression levels of the gene of interest relative to the housekeeping gene, GAPDH using the formulae below:

ΔCt = Ct (gene of interest) – Ct (housekeeping gene) $\Delta\Delta Ct = \Delta Ct$ (sample group) - ΔCt (control group)

Relative Expression = $2^{-\Delta\Delta Ct}$

After calculating gene expression relative to the housekeeping gene, GAPDH, unless stated otherwise, values for three biological replicates were averaged and unpaired, two-tailed, parametric *t*-tests were performed to calculate the significance of any differences between control and treated samples. *P* values of <0.05 were considered as statistically significant.

Total Protein Extraction

Total protein was extracted from cells by first harvesting ~2 x 10^6 cells by centrifuging at 1200rpm for 5 minutes. Cell pellets were washed with 1ml PBS and centrifuged again as before. As much PBS as possible was removed from the pellets before re-suspending in ~80ul lysis buffer (20mM Tris, pH 7.5, 150mM NaCl, 10mM EDTA, 0.5% deoxycholic acid, 0.5% Triton X-100). 1 protease inhibitor tablet (Roche, Cat. 04693159001) was added to 10ml lysis buffer immediately before use. Samples were then homogenized using a 1ml syringe and needle (21G x 1.5" – Nr.2., 0.8mm x 40mm) and incubated on ice for 30 minutes before centrifuging at 14,000rpm for 20 minutes at 4°C. The resulting supernatant was pipetted into a fresh, sterile eppendorf and stored at -20°C.

Nuclear and Cytosolic Protein Extraction

Approximately 1.5 x 10^7 cells were harvested by centrifuging at 1200rpm for 5 minutes at room temperature and washed in PBS. As much supernatant was removed from the pellet as

possible, which was then re-suspended in 150ul cold Buffer RLN and incubated on ice for 10 minutes. One protease inhibitor tablet (Roche, Cat. 04693159001) was added to 10ml Buffer RLN immediately before use. The mix was centrifuged at 3700 rpm for 5 minutes at 4^{o}C and 100ul supernatant was transferred to a new eppendorf (cytosolic fraction). The remainder of the supernatant was discarded, and the pellet was washed twice with 100ul Buffer RLN, centrifuging between washes as before. The resulting pellet was re-suspended in ~80ul lysis buffer. One protease inhibitor tablet (Roche, Cat. 04693159001) was added to 10ml lysis buffer immediately before use. Samples were then homogenized using a 1ml syringe and needle (21G x 1.5" – Nr.2., 0.8mm x 40mm) to lyse nuclei, and incubated on ice for 30 minutes before centrifuging at 14,000rpm for 20 minutes at 4^{o}C. The resulting supernatant was pipetted into a fresh, sterile eppendorf (nuclear fraction) and stored at -20^{o}C.

Histone Protein Extraction

10^{7} cells were harvested for histone extraction. Cells were first lysed in 500ul histone extraction buffer (PBS containing 0.5% Triton X-100, 2mM phenylmethylsulfonyl fluoride, 0.02% sodium azide) for 1 minute on ice, followed by centrifuging at 8000rpm for 10 minutes at 4^{o}C. The resulting pellet was washed in 250ul histone extraction buffer and centrifuged as before. The pellet was then resuspended in 0.4M HCl and incubated overnight at 4^{o}C for acid extraction of histones. The following morning, samples were centrifuged as before and the supernatant (containing histone protein) was saved. The HCl was neutralized by adding 0.1X volumes of 2M NaOH. The histone protein was then used in SDS- PAGE (2.7.6). All histone extractions were performed in collaboration with Dr John Halsall (Institute of Cancer and Genomic Sciences, University of Birmingham) (Halsall et al., 2015)

Bradford Assay Protein Quantification

To ensure equal loading of samples in SDS-PAGE, protein concentrations were determined via Bradford assay. Standard samples (5ul of known BSA protein concentration in serial

dilution ranging from 0-2mg/ml) and 5ul of experimental protein samples were loaded in duplicate into a 96-well plate along with 250ul Bradford reagent (Sigma, Cat: B6916). Absorbance was measured at 570nm using a Tecan infinite 5200 pro plate reader and iControl^{TM} Microplate Reader Software. A standard curve was plotted from the standard samples of known protein concentration (conc. vs absorbance). The protein concentration of the experimental samples was determined by subtracting the absorbance from a blank control absorbance value, and then dividing by the slope of the standard curve.

Immunoblotting

For SDS-PAGE, 10% polyacrylamide SDS resolving gels (6.66ml 30% acrylamide, 5ml 1.5M Tris pH8.8, 200ul 10% SDS, 200ul 10% APS, 20ul TEMED and 8ml H_2O) were prepared with a 4% stack (1.7ml 30% acrylamide, 2.5ml 0.5M Tris pH6.8, 100ul 10% SDS, 100ul 10% APS, 20ul TEMED and 5.55ml H_2O) and stored in moist wrapping at 4°C for no more than 1 week before use.

Before loading onto gels, extracted protein samples were mixed with 5X SDS loading dye (200mM Tris-HCL pH6.8, 40% glycerol, 4% SDS, 0.4% bromophenol blue, 200mM β-mercaptoethanol) and heated at 70°C for 10 minutes. In addition to protein samples, 3ul of protein ladder (PageRuler^{TM} Plus Prestained Protein Ladder, ThermoFisher Scientific, Cat: 26619) was loaded onto gels as a molecular weight marker for use as a size standard reference. Gels were then run for approximately 90-120 minutes at 120V in cold 1X Running Buffer (100ml 10X running buffer, 5ml 20% SDS, 895ml dH2O) (10X running buffer: 60g Tris, 288g glycine, up to 2L dH_2O).

After running, a semi-dry transfer was performed onto nitrocellulose membranes using the Trans-Blot Turbo Transfer System (BIO-RAD, Cat. 1704271) and 1X Transfer Buffer (200ml BIO-RAD TransBlot Turbo 5 x Transfer Buffer (Cat. 1704271), 200ml 100% Ethanol, 600ml nanopure H2O). Membranes were then blocked in 5% skimmed milk in TBS for 1 hour before incubating in primary antibody overnight at 4°C, with agitation. All primary antibodies (Table S2) were prepared in 5% BSA. The following morning, the membranes were washed three

times in TBS-T for 5 minutes and incubated in the appropriate secondary antibody (Table S3), diluted in blocking solution (5% skimmed milk in TBS-T) in the dark for 1 hour, at room temperature, with agitation. The antibody was removed, and the membranes were washed twice in TBS-T for 5 minutes, and once in TBS for 5 minutes for a final time, before storing in TBS at 4°C.

Membranes were scanned and protein bands were detected using the Odyssey infrared detection system (LI-COR Biosciences). Images were then analyzed and the protein bands were quantified using Image Studio Lite software.

DNA methylation analysis using bisulphite sequencing

For DNA methylation analysis, 1 mg of genomic DNA was sodium bisulphite converted using the EZgold DNA methylation kit (Zymoresearch) following the supplier's protocol and eluted in 50 ml of 1mM Tris-HCl pH 8.0, 0.1mM EDTA. Three ml from this eluate were used for each PCR amplification to prepare the pyrosequencing template, using the PyroMark PCR Kit (Qiagen). PCR volume was 30 ml containing 200 nM of each forward and reverse primer (Table S4). Primers were designed using the Pyromark Assay Design 2.0 software (Qiagen). The thermal profile included an initial denaturation step at 95ºC for 15 min, followed by 40 cycles consisted of 94ºC for 30 sec, 52ºC for 30 sec and 72ºC for 30 sec. A final extension step at 72ºC for 20 min was utilised. Following quality control of the PCR products on a 2% agarose gel, DNA methylation was measured by Pyrosequencing using the PyroMark Gold Q96 SQA Reagents and a Pyromark Q96 ID instrument (Qiagen), following the manufacturer's protocol. Methylation levels (%) are calculated per CpG site using the Pyromark Q96 2.5.8 software (Qiagen). Methylation index (MtI) represents the mean value of all the CpGs in a target sequence per sample. The difference of DNA methylation between cell lines was tested using the Friedman's non-parametric test, using SPSS 25.0 software.

DNMT1 RNA Immunoprecipitation (RIP)

2×10^7 cells were harvested per RIP. Cell pellets were washed in PBS three times and resuspended in 500ul ice-cold Buffer RLN (containing 100U/ml RNase inhibitor and with 1 protease inhibitor tablet added to 10ml RLN). This was incubated on ice for 10 minutes before centrifuging at 3700rpm, for 5 minutes at 4°C. Nuclear pellets were washed with 100ul Buffer RLN, followed by resuspending in 500ul freshly prepared RIP Buffer (25mM Tris, pH 7.4, 5mM EDTA, 150mM KCl, 0.5mM DTT, 0.5% NP40 Igepal, 100U/ml RNase inhibitor) with added protease inhibitor. This mix was incubated on ice for 3 hours with frequent, gentle agitation. Following the incubation, nuclei were homogenized using a 1ml syringe and needle (21G x 1.5" – Nr.2., 0.8mm x 40mm), then centrifuged at maximum speed for 10 minutes at 4°C to pellet nuclear debris. The supernatant was kept and transferred to an RNase- free eppendorf, to which 6ug of either DNMT1 of IgG (control) antibody was added (Table S2). This mix was incubated overnight at 4^{O}C with gentle rotation.

The following day, 50ul (1.5mg) magnetic beads (Dynabeads Protein G Immunoprecipitation kit, Invitrogen, Cat: 10007D) were prepared per RIP. Similar to 2.8, the beads were placed into an eppendorf on a magnetic separator and the supernatant was removed. This was followed by two washes with 100ul RIP buffer. The overnight antibody-protein-RNA suspension was added to the beads and incubated for 1 hour with gentle rotation at 4°C. Following this incubation, the beads- antibody-protein-RNA were placed on the magnet, the supernatant was removed, and the complex was washed three times with 500ul ice-cold RIP buffer and once with RNase-free PBS. At this point, 5% of the bead slurry was collected to be used in SDS-PAGE analysis to confirm DNMT1 pull-down. The remaining beads- antibody-protein-RNA was resuspended in 100ul RIP buffer with 50ug proteinase K and 0.1% SDS. This was incubated at 55°C for 45 minutes to detach the protein- RNA complexes from the beads. The eppendorf was then placed onto the magnet and the supernatant was transferred to a new eppendorf. The beads were discarded.

To purify the RNA, 1X volume of phenol-chloroform-isoamyl alcohol was added to the supernatant and vortexed thoroughly. This was phase separated by centrifuging at 14,000rpm for 10 minutes at 4°C. The aqueous phase (containing the RNA) was carefully collected and placed into a fresh eppendorf. Any remaining aqueous phase was further extracted by the addition of 150ul back extraction buffer (10mM Tris, pH8, 1mM EDTA, 100mM NaCl, 0.25% SDS), followed by vortexing and centrifugation as before. Any remaining aqueous phase was collected and added to the previous collection.

The RNA was further purified by ethanol precipitation. 0.1X volumes of 3M sodium acetate (pH 5.2), 2.2X volumes of 100% ice cold ethanol and 1ul glycogen was added to the RNA extract and incubated at -20°C overnight. The following morning, the mix was centrifuged at 10,000rpm for 20 minutes at 4°C and the supernatant carefully discarded. 500ul 70% ice cold ethanol was added, and the mix centrifuged as before. The ethanol was carefully removed, and the tubes were left open to allow any residual ethanol to evaporate. The purified RNA was then finally dissolved in 20ul RNase-free H_2O. This RNA was then DNase-treated and converted into cDNA, and qRT-PCRs were performed. Results were analysed using the calculations below to determine DNMT1 enrichment for *CCDC26* compared to the IgG control.

DNMT1 RIP ΔCt = Ct DNMT1_RIP_CCDC26 – Ct INPUT_RNA_CCDC26

IgG RIP ΔCt = Ct IgG_RIP_CCDC26 – Ct INPUT_RNA_CCDC26

$\Delta\Delta$Ct = DNMT1 RIP ΔCt – IgG RIP ΔCt Relative Expression = $2^{-\Delta\Delta Ct}$

RNA-sequencing and metagene analyses

RNA-sequencing was carried out on RNA extracted from wild-type K562 cells and CCDC26 KO K562 cells. The sequencing was carried out on three biological triplicates. RNA-sequencing libraries were prepared using TrueSeq method. All the libraries were paired-end sequenced on an Illumina HiSeq 2500 machine (University of Birmingham). Sequences were quality filtered and trimmed using cutadapt. The reads were mapped using TOPHAT package

(Trapnell et al., 2009) against human genome (hg19). Differential analysis was done using cuffdiff programme. Differential genes were identified using false discovery cut-off of 1×10^{-5} and used for further analysis. The sequencing data is deposited GEO database (accession no. GSE105029) Metagene plots and heatmap were generated using DeepTools package(Ramirez et al., 2014). DNA methylation metagenes were generated using K562 MeDIP data deposited in ENCODE database (GEO: GSE56774). The GC heatmap were created using previously calculated GC content track for human genome available from UCSC genome browser (http://hgdownload.cse.ucsc.edu/goldenPath/hg19/gc5Base/).

REFERENCES

Halsall, J.A., Turan, N., Wiersma, M., and Turner, B.M. (2015). Cells adapt to the epigenomic disruption caused by histone deacetylase inhibitors through a coordinated, chromatin-mediated transcriptional response. Epigenetics Chromatin *8*, 29.

Ramirez, F., Dundar, F., Diehl, S., Gruning, B.A., and Manke, T. (2014). deepTools: a flexible platform for exploring deep-sequencing data. Nucleic acids research *42*, W187-191.

Trapnell, C., Pachter, L., and Salzberg, S.L. (2009). TopHat: discovering splice junctions with RNA-Seq. Bioinformatics *25*, 1105-1111.